water

MDPI

Article

Optimizing Electrocoagulation-Adsorption Treatment System for Comprehensive Water Quality Improvement in Olive-Mill-Wastewater (OMW): Synergy of EC Utilizing Al Electrodes and Olive Stones Biochar as a Sustainable Adsorbent

Ahmad Jamrah [1,*], Tharaa M. Al-Zghoul [1], Zakaria Al-Qodah [2], Emad Al-Karablieh [3], Maram Mahroos [4] and Eman Assirey [4,*]

[1] Department of Civil Engineering, School of Engineering, The University of Jordan, Amman 11942, Jordan; tharaaalzghoul@gmail.com
[2] Department of Chemical Engineering, Faculty of Engineering Technology, Al-Balqa Applied University, Amman 11134, Jordan; zak@bau.edu.jo
[3] Department of Agricultural Economics and Agribusiness, School of Agriculture, The University of Jordan, Amman 11942, Jordan; karablie@ju.edu.jo
[4] Chemistry Department, Faculty of Science, Taibah University, Madinah P.O. Box 41411, Saudi Arabia; Tu4570549@taibahu.edu.sa
* Correspondence: jamrah@ju.edu.jo (A.J.); eassirey@taibahu.edu.sa (E.A.)

Abstract

This research employed "Response Surface Methodology (RSM)" to assess the effectiveness of electrocoagulation (EC) in treating olive mill wastewater (OMW) before applying adsorption with olive stone biochar (OS) as a sustainable adsorbent. Several parameters, including reaction time, current density (CD), inter-electrode distance, and the number of electrodes, were optimized. Analysis using Minitab 22.2 resulted in robust regression models with high coefficients of determination (R^2). The optimal parameters were CD of 12.41 mA/cm^2, a time of 45.61 min, an inter-electrode spacing of 1 cm, and a maximum of 6 electrodes, resulting in an energy consumption (*ENC*) of 9.85 kWh/m^3. Significant pollutant percentage removals were achieved: 72.32% for total Kjeldahl nitrogen (TKN), 80.74% for turbidity, 57.44% for total phenol (TPh), 56.9% for soluble chemical oxygen demand ($COD_{soluble}$), and 56.6% for total chemical oxygen demand (COD_{total}). After the EC, the adsorption of pollutants was conducted using OS biochar that was generated through the pyrolysis of OS at a temperature of 500 °C. FTIR analysis of the biochar revealed key absorption bands that indicated the presence of inorganic compounds, aromatic C=C, and phenolic groups O-H. The integrated EC and adsorption (ECA) process demonstrated markedly higher efficiencies, with TPh removal reaching 61.41%, turbidity reduction at 81.92%, TKN reduction at 77.78%, $COD_{soluble}$ reduction at 70.31%, COD_{total} reduction at 65.1%, and project cost of \$2.88/m^3. The ECA process presents a promising treatment approach for OMW.

Keywords: electrocoagulation; adsorption; response surface methodology (RSM); olive mills wastewater (OMW); olive stone biochar (OS); sustainable adsorbent

Check for updates

Academic Editor: Christos S. Akratos

Received: 13 October 2025
Revised: 2 January 2026
Accepted: 9 January 2026
Published: 13 January 2026

1. Introduction

Today, the world is confronted with significant challenges related to water scarcity and pollution, driven by rapid population growth and urbanization [1]. This situation

https://doi.org/10.3390/w18020212

places immense pressure on water availability and quality, affecting both developing and developed nations alike [2,3]. While developing countries often face acute water shortages, industrial pollution has exacerbated water scarcity in developed regions as well [1]. The global urban population facing water scarcity is projected to potentially reach between 1.7 and 2.4 billion people by 2050, highlighting the significance of the "United Nations Sustainable Development Goal 6," which aims to guarantee access to clean water and sanitation for everyone [4]. The consequences of water pollution are severe, and caused about 1.6 million deaths in 2018 according to the "World Health Organization (WHO)" [5,6]. Various industries contribute significantly to wastewater production, including car washes [7], pharmaceuticals [8], dairy [9], textiles [10], and petroleum refining [11]. The discharge of toxic and non-biodegradable substances from these wastewaters poses serious threats to the environment and public health [12].

A noteworthy source of wastewater pollution is the olive oil industry, particularly through the discharge of olive mill wastewater (OMW) [13]. The global production of OMW is estimated at 40 million m^3 annually, with Mediterranean countries responsible for over 75% of this output, producing around 30 million m^3 per year [14,15]. For each ton of processed olives, approximately 1.3 m^3 of wastewater is generated [16]. In Jordan alone, the olive oil sector produced about 24,000 tons of olive oil in 2022, resulting in 300,000 m^3 of OMW, known locally as "Zibar," along with 120,000 tons of solid waste by-product referred to as "Jift" [2,8]. OMW poses several health and environmental risks, including the pollution of water bodies and groundwater [17], harm to agricultural lands [18], and adverse effects on ecosystems [19]. OMW is characterized by its high toxicity and complex composition, containing variable levels of suspended solids, organic matter, proteins, and phenolic compounds impacted by factors such as climatic conditions and cultivation methods, and the followed extraction method (continuous centrifugal and traditional intermittent pressing methods) [2,15].

The treatment of OMW is complicated due to its recalcitrant nature, which hinders biodegradability and increases treatment costs [20,21]. OMW is notable for its acidic characteristics, with pH values of 2.2 to 6 [15,22]. It has a high "biological oxygen demand (BOD)" that varies from 32.1 to 132 g/L and a "chemical oxygen demand (COD)" between 30 and 320 g/L [22]. Additionally, OMW contains total suspended solids (TSS) ranging from 1 to 120 g/L, along with significant amounts of organic matter, residual fats, and "total phenols (TPh)" of values from 0.5 to 24 g/L [15,22]. These values can vary based on the specific olive mills and the extraction processes utilized [2]. Consequently, it is essential to manage the OMW before discharging it into the environment or public sewage systems [23,24]. The treatment of OMW typically includes biological, chemical, and physical methods tailored to the unique properties of the water and the pollutants present [2]. Common techniques include aerobic and anaerobic processes [25,26], advanced oxidation [27], membrane filtration [28,29], and coagulation/flocculation [30]. However, due to their significant limitations, including their relatively high cost, low biodegradability, and complexity, these processes are unable to meet the necessary standards [31,32]. Accordingly, there is an increasing need to develop efficient, cheap, and straightforward approaches for OMW treatment [2].

One promising method is electrocoagulation (EC), which has been effectively used to treat water and wastewater containing both inorganic and organic contaminants [33]. This method relies on generating aluminum (Al) ions from Al electrodes, which act as coagulants. During the electrocoagulation process, the former flocs settle, while hydrogen gas evolving at the cathode may cause some flocs to float to the surface [31,34]. The EC advantages include the lack of chemical additives, versatility, simplicity, quick startup, ability to handle various contaminants, and ease of sludge collection [35,36]. Moreover, combining the EC treatment step with other processes will result in a significant improvement in the pollutant percentage removal [2,37]. Research has shown that integrated methods, such as EC and adsorption (ECA), were able to enhance the percentage removal by 20% more than using EC alone [38]. This combined approach can yield highly purified treated wastewater, promoting effective water reuse [9]. The adsorption process is characterized by its percentage removal and low energy requirements. Some studies have reported percentage removal of 99.9% for both soluble and suspended pollutants [9,39]. This process is particularly valued for its minimal space requirements, low initial costs, and simplicity compared to other treatment options [39]. Actually, the use of low-cost inexpensive local adsorbents, such as natural materials, has received increasing interest [39]. In Jordan and other countries, olive stone biochar (OS) is produced as a by-product after olive oil centrifugation. This solid material, known locally as "Jift," presents a cheap source for "activated carbon (AC)" production [40]. Jift or its biochar has demonstrated its ability to adsorb many ions and compounds found in ground and wastewater [41]. These characteristics suggest that using this local bio-waste as adsorbent will minimize their disposal management costs and will provide an additional cost-effective source for AC [42,43].

Recently, several experimental design models have been applied in research to enhance methodologies, decrease time, minimize energy usage, and analyze the impacts of different variables on the process performance [44,45]. Key statistical methods employed for this purpose include "Response Surface Methodology (RSM)." Within RSM, the "Central Composite Design (CCD)" is particularly effective, as it provides sufficient data to evaluate the validity of the experimental model and lows for accurate estimation of quadratic and interaction effects, making it suitable for the current case [46,47].

This research intends to optimize OMW treatment by combining the EC and adsorption processes. The performance of EC was evaluated by examining the removal of turbidity, COD, "Total Kjeldahl Nitrogen (TKN)," TPh, and "energy consumption (*ENC*)." The adsorption step utilizing OS was conducted as a post treatment step to further reduce pollutants. The combined ECA system was evaluated using RSM to determine the key factors affecting contaminant removal. The CCD was applied to investigate the impact of some key parameters, such as number of electrodes (N) (2, 4, and 6), distance between the electrodes (D) (1, 2, 3, and 4 cm), current density (CD), and reaction time (t) on the percentage removal of pollutants. This study indicates that optimizing the EC and adsorption processes can improve the efficiency, cost-effectiveness, and sustainability of treating highly polluted industrial wastewater. The findings present practical guidelines for reducing energy consumption, minimizing electrode passivation, and enhancing contaminant removal. These enhancements could support the broader application of these technologies in industrial settings.

2. Experimental Work

2.1. OMW Collection

In this study, OMW samples were obtained from a mill in Ajloun city, Jordan. This mill utilizes a "three-phase extraction" method. OMW sample collection took place in the olive harvesting period between October and December 2023. Notably, such mill operation processes include no added chemicals. This indicates that the produced OMW samples accurately represent the natural properties of the effluent. Samples were collected during two distinct periods: the first sample (OMW I) was collected in early October 2023 at the beginning of the olive harvest, and the second sample (OMW II) was collected in December 2023 at the end of the harvest season. The processes utilized for sampling, conditioning, and storing the samples are crucial as they significantly affect the samples' analysis and their interpretation.

To maintain their initial quality, the OMW samples extracted from the OMW storage basin were filled in 20 L plastic vessels and then stored at 4 °C. Prior to OMW sample treatment, suspended solids were decanted and filtered using a cloth filter. This precleaning step was important to remove solids to ensure that the adsorption process was performed only by the adsorbent particles added to the clean OMW. This methodology improves the applicability and relevance of the research's outcomes to possible future large-scale treatment applications.

2.2. Chemicals

All chemicals used in this research were of analytical grade. They were obtained from "Alnoorien Est. for Laboratories & Scientific Supplies in Amman, Jordan," including "boric acid" (4%), "sodium hydroxide" (1 N NaOH), "copper sulfate ($CuSO_4$)," and "potassium sulfate (K_2SO_4)." Additional chemicals, such as "2-Chloro-6-(trichloromethyl) pyridine ($C_6H_3Cl_4N$)," "potassium hydroxide (KOH)," and "a COD kit HR (0–15,000 mg/L)," were sourced from "Hilmi Abu Sham and Partners Company in Amman, Jordan". Other reagents acquired from the same source include "sulfuric acid (1 N H_2SO_4)," "ethanol (C_2H_6O)," "hydrochloric acid (0.1 M HCl)." In addition, "potassium nitrate (KNO_3)," "sodium chloride (NaCl)," and "potassium hydrogen phthalate (KHP)" were also purchased from this supplier. Lastly, the "Folin–Ciocalteu reagent," "anhydrous sodium carbonate (Na_2CO_3)," and "dry gallic acid (GA)" were purchased from "Sidor Company in Irbid, Jordan."

2.3. Methodological Approaches in Environmental Analysis

To enhance the reliability and accuracy of the research, outcomes obtained from "the Environmental Engineering Laboratory" were cross-validated with other analytical laboratories. This verification method was essential for ensuring adherence to the highest quality standards, as the outcomes of these tests were critical for guiding important recommendations.

2.3.1. Evaluation of Quality Parameters

To evaluate the performance of the ECA processes, several quality variables were measured. These parameters include turbidity, TKN, TPh, "soluble chemical oxygen demand ($COD_{soluble}$)," and "total chemical oxygen demand (COD_{total})."

2.3.2. Instrumentation

The pH and temperature were measured using a "HAANA pH Meter (Hanna HI 2002-02, Hanna Instruments, Woonsocket, RI, USA)." Electrical conductivity was measured with a "Delta OHM meter (HD 3406.2, Delta OHM, Selvazzano Dentro, Italy)," in mS/cm, while turbidity was assessed with a "Velp Scientifica TB1 turbidity meter," in NTU. In addition, an analytical balance from "BEL Engineering" with a precision of 0.001 g was used for precise mass measurements. These parameters were measured at the beginning of each experiment.

COD was measured utilizing a "spectrophotometer (HACH Lange DR 3900, Hach Company, Loveland, CO, USA)," in mg/L, and BOD test was performed according to Winkler methods using a "magnetic stirrer (Velp F20500051 Heating Magnetic Stirrer AREC.T, Velp Scientifica, Jakarta, Indonesia)," in mg/L. Both tests followed procedure outlined by Jamrah et al. [48] and Baird et al. [49], respectively.

The TPh content was assessed using the "Folin–Ciocalteu Method," in mg/L as gallic acid equivalent, with the same spectrophotometer at a wavelength of 765 nm. This method involves mixing the sample with the Folin–Ciocalteu reagent and sodium carbonate to develop color for adsorbance measurement [50].

https://doi.org/10.3390/w18020212

The TN content was measured utilizing the "macro-Kjeldahl process," which determines ammonium and organically bound nitrogen. The sample was digested at specific temperatures using a "Velp digestion block," followed by distillation in a "Velp distillation unit." Ammonium was converted to ammonia and captured in boric acid, then titrated with 0.01 M H_2SO_4. The calculations for Kjeldahl nitrogen are based on the volumes and normality of the solutions used [51].

2.4. The Combined ECA

This study implemented a two-stage integrated process, utilizing EC as the initial process followed by an adsorption step. This treatment system is expected to achieve high pollutants percentage removal and clean remediated wastewater.

2.4.1. The EC Method

The lab-scale EC unit featured a rectangular plastic reactor with a working volume of 3 L. The dimensions of the Al electrodes were 10 cm × 6 cm and 2 mm thickness, and they were immersed to a depth of 4 cm, enabling effective flow of effluent between the plates. The electrodes, crafted by a "local blacksmith," were configured in a monopolar series (MP-S) configuration, consisting of three anodes Al and three Al cathodes. To ensure stability and vertical alignment, wooden spacers were attached to the electrodes. A mixer operated at 350 rpm to provide homogeneous solution. The power for the EC cell was supplied by a DC generator "(Sunshine-P-3005 A)." To improve electrical conductance and minimize *ENC*, 1000 mg/L of NaCl was added. After treatment, the treated solution was allowed to settle. Figure 1 provides a representation of the reactor utilized in the EC process.

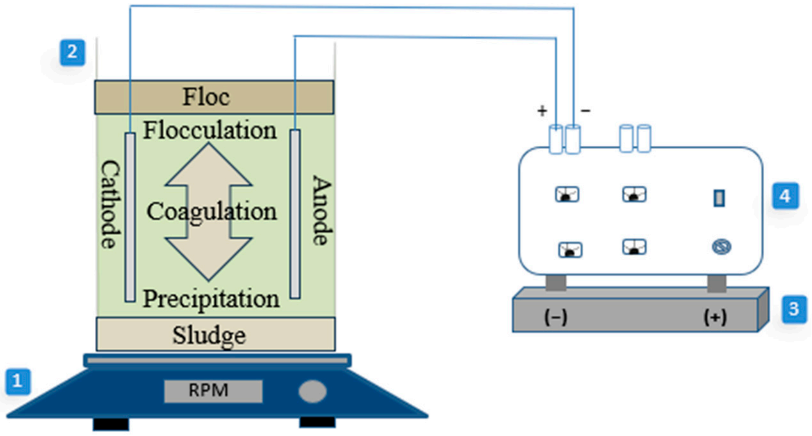

Figure 1. Schematics of the EC method: 1, a stirrer; 2, an EC reactor; 3, a battery; 4, a DC power supply.

Aluminum Electrodes

As previously mentioned, Al was utilized as the electrode material. The following chemical reactions indicate the formation of $Al(OH)_3$, as described in Equations (1)–(3), which then coagulates the contaminants present in OMW [52]:

$$\text{Anode} : \text{Al} \rightarrow \text{Al}^{3+} + 3\text{e}^- \tag{1}$$

$$\text{Cathode} : 3\text{H}_2\text{O} + 3\text{e}^- \rightarrow \frac{3}{2}\text{H}_2 + 3\text{OH}^- \tag{2}$$

$$\text{Overall} : \text{Al}^{3+} + 3\text{H}_2\text{O} \rightarrow \text{Al(OH)}_3 + 3\text{H}^+ \tag{3}$$

In each experiment, an OMW sample was placed into the EC reactor. The EC method was evaluated under a range of conditions, including contact times of 5 to 65 min, applied currents of 1 to 5 A, inter-electrode distances of 1 to 4 cm, and the number of Al electrode pairs of 1 to 3. Throughout the experiments, some particles precipitated onto the electrodes. At the end of each experiment, the electrode surfaces were cleaned using a 0.1 M HCl solution (Hilmi Abu Sham and Partners Company in Amman, Jordan) to remove the sludge and then rinsed with distilled water. The electrodes were then refurbished through sanding, cleaning, and removing the oxide layer. After drying, they were weighed to assess the overall operating cost for each run. The restored electrodes were kept for future use. Samples were withdrawn from the bottom of the EC cell using a pipette, and then filtered prior to analysis. This procedure was systematically repeated across all experimental conditions. The effective area of the electrodes was 240 cm^2 (10 cm × 4 cm × 2 sides' × 3 anodes or cathodes).

Equation (4) was used to calculate the results of the treatment of OMW using Tivalent/L Followed By EC, and EC Followed By SBR. The percentage removal (R%) was calculated as follows [50]:

$$R(\%) = \frac{(C_0 - C_e)}{C_0} * 100 \tag{4}$$

where C_e and C_0 are the final and initial concentrations of the pollutant such as COD (mg/L), respectively.

Adsorption Process

The adsorption step was employed as a post-polishing stage, using biochar generated from OS. This integrated system offers a sustainable and cost-effective solution, as biochar demonstrates a high adsorption capacity for efficiently removing pollutants from effluents [40]. While the EC process efficiently addresses larger contaminants, the next adsorption step targets any remaining contaminants. The kinetics of adsorption were investigated utilizing a batch method, with a focus on parameters such as particle size. The shaking duration was standardized at 3 h at a speed of 200 rpm, with the exception of the experiment that examined the effect of contact time, where the shaking durations were varied. All runs were conducted 20 °C following agitation. Samples were taken as in the previous EC step.

Preparation of Biochar Adsorbent from Olive Stones

The biochar production process from OS granules, obtained from olive mills in Ajloun city, Jordan, as described in our study [48], included several steps. The OS granules were first washed with distilled water to remove any attached impurities. Then, OS was dried for 24 h in an oven at 50 °C. The dried OS was then sieved using a 4.75 mm sieve to remove any residual stones or leaves. Samples of 100 g of the dried OS were wrapped in aluminum foil and subjected to heating in "a muffle furnace" "Nabertherm, Lilienthal, Germany" at three different temperatures (400, 500, and 600 °C) for varying durations of 1 to 5 h to determine the optimal conditions for biochar production. After pyrolysis, the produced biochar was ground using a grinder "Silver Crest, Hong Kong, China, SC-1880" and subsequently sieved with an electric shaker "Matest S.p.A., Treviolo, Italy, Electromagnet A059-02KIT" to obtain three fractions: 0.075 mm, 0.15 mm, and 0.3 mm. The resulting biochar fractions were then stored in glass bottles for further use.

Properties of Biochar

In the current study, we conducted the same tests as in our previous research [48], following the established methodologies. The biochar was characterized by evaluating percentage yield, electrical conductivity, ash content, and zeta potential. The zeta potential measurements were taken at the pH of OMW to accurately reflect the conditions relevant to its application. Additionally, we performed "Fourier Transform Infrared Spectroscopy

(FTIR)" and morphological examination using SEM were all performed using the same protocols as in our previous research [48]. Lastly, "X-ray diffraction" "XRD" analysis was also conducted with an "AERIS X-ray diffractometer" "Malvern Panalytical, Almelo, The Netherlands".

Adsorption Kinetics Experiments

In this study, we conducted adsorption kinetics experiments to evaluate the removal efficiency of pollutants (TPh, $COD_{soluble}$, COD_{total}, TKN, and turbidity) from OMW using biochar as the adsorbent. A set of four tubes was prepared, each filled with the same volume of adsorbate solution at varying initial concentrations. A constant mass of 0.1 g of biochar was added to each tube, along with glass beads to enhance mixing. The tubes were then shaken at a speed of 200 rpm for specified durations: 5, 10, 15, 20, 30, 60, 90, 120, 150, and 180 min.

Throughout the shaking intervals, tests were conducted to monitor the changes in concentration of TPh, $COD_{soluble}$, COD_{total}, TKN, and turbidity. These measurements were crucial for assessing the overall removal efficiency of the biochar in removing pollutants from the solutions. The results obtained from these kinetic experiments highlight the significant impact of particle size on pollutant removal efficiency, underscoring the importance of optimizing particle size for effective treatment of OMW.

2.5. Criteria for Response Evaluation in CCD

To determine the optimal parameters for the removal of COD_{total}, $COD_{soluble}$, TPh, TN, turbidity, and *ENC*, "Minitab 22.2 software" was used to perform RSM with CCD aimed at optimizing the EC method. The continuous variables selected for the experimental design included a CD ranging from 4.17 to 20.8333 mA/cm^2, a reaction time varying between 5 and 65 min, and an electrode spacing of 1 to 4 cm. Additionally, the categorical variable selected for the experimental design included the number of electrodes, which used in previous studies [53,54]. Table 1 shows the input variables and their values in minimum, medium, maximum, and coded values.

Table 1. Input variables and their levels for experimental design.

Variables	Minimum	Medium	Maximum	Coded Low	Coded Medium	Coded High
Electrode Spacing (cm)	1	3	4	−1.68179	0	+1.68179
Reaction Time (min)	5	27.5	65	−1.68179	0	+1.68179
CD (mA/cm^2)	4.17	12.5	20.833	−1.68179	0	+1.68179
Electrode Number	2	4	6	1	2	3

Using "Minitab 22.2," a CCD, which was built with the mentioned parameters and their levels to create a design matrix with a total of 60 runs. An "analysis of variance" "ANOVA" was performed to evaluate the statistical significance for samples and means. Initially, linear regression models were fitted to the data to create a mathematical relation between the influencing factors and the response variables. Following this, second-order regression was employed to improve the model by incorporating interaction and quadratic terms. The model's significance and importance were compared using ANOVA.

Coded values are usually utilized instead of the original units of the factors during data analysis and interpretation. This is due to the different numerical results that can be obtained when using the original units, the difficulty of interpreting the results, and the difficulty of interpreting the interaction between the variables. Coded values are also more effective in determining the relative size of the effects of the factors. The relationship between the original and coded values is defined by Equation (5) below [55]:

$$\text{Coded Value} = \frac{\text{Actual Value} - \text{Mean of the Low and High Values}}{\text{The difference between the Low and High Values}} \tag{5}$$

A "2nd order polynomial" is utilized to build functional relationships between the response variables and the influencing factors. The relationship is expressed in Equation (6) [55]:

$$\text{Response} = \mathrm{a_0} + \sum_{\mathrm{i=1}}^{\mathrm{n}} \mathrm{a_i X_i} + \sum_{\mathrm{i=1}}^{\mathrm{n}} \mathrm{a_{ii} X_i}^2 + \sum_{\mathrm{i<j}}^{\mathrm{n}} \sum_{\mathrm{j}}^{\mathrm{n}} \mathrm{a_{ij} X_i X_j} + \beta \tag{6}$$

where "$\mathrm{a_0}$ represents the constant coefficient, ai the linear coefficient, $\mathrm{a_{ii}}$ the quadratic coefficient, $\mathrm{a_{ij}}$ the interactive coefficient, X denotes the uncoded values of the factors, and β is the error term".

2.6. Cost Analysis of the EC

For each run, the current and voltage readings were recorded. One of the response variables, energy consumption (*ENC*), is estimated utilizing these measurements. Equation (7) is employed to calculate *ENC* [56]:

$$ENC\left(\frac{\text{KWhr}}{\text{m}^3}\right) = \frac{\text{VIt}}{\text{Volume of Sample}} \tag{7}$$

where "I is the applied current in A, t is the time in h, and V is the voltage in volts".

Electrode consumption ($ELC_{theoretical}$) is calculated according to Equation (8) [57]:

$$ELC_{theoritical}\left(\frac{\text{kg}}{\text{m}^3}\right) = \frac{It_{EC}M_W}{ZFV} \tag{8}$$

where $ELC_{theoretical}$ is the theoretical electrode consumption in kg/m^3," the applied current is denoted by I in A, while t_{EC} indicates the duration of the EC process in seconds. The chemical equivalence of the electrode is represented by Z, which has a value of 3 for Al ($Z = 3$). Additionally, Faraday's constant is represented by F, with a value of 96,500 C/mol for Al, M_W stands for the molecular weight of the electrode metal, which is 27 g/mol for Al. Finally, V indicates the volume of the treated wastewater in m$^{3"}$.

The actual amount of electrode consumption (ELC_{actual}) was calculated as follows [57]:

$$ELC_{actual}\left(\frac{\text{kg}}{\text{m}^3}\right) = \frac{\left(m_i - m_f\right)}{v} \tag{9}$$

where ELC_{actual} is the consumed number of electrodes per unit volume of pharmaceutical wastewater sample (kg/m^3), m_i is the initial weight of electrodes (kg), m_f is the final weight of electrodes after treatment (kg), and V is the volume of the OMW sample (m^3).

The "operating cost (*OPC*)" for OMW treatment can be estimated by the following Equation [58]:

$$OPC = aENC + bELC + cCHC + Biochar\ Cost + Sludge\ Cost \tag{10}$$

where *OPC* is the total operational cost of EC in \$/m^3. The variable *CHC* refers to the consumption of the neutralizing chemical, measured in kg/m^3. The coefficient a denotes the price of electrical energy per kilowatt-hour (\$/kWh), while b corresponds to the cost of the electrodes in \$/kg. The variable c indicates the price of biochar, also expressed in \$/kWh.

The Biochar Cost is calculated based on the quantity of biochar used for treating one m^3 of wastewater, multiplied by its unit price. For instance, if the cost of biochar is approximately \$0.00467/m^3, this value is incorporated directly into the equation. Similarly, the Sludge Cost accounts for the expenses associated with the treatment and disposal of the sludge generated during the treatment process. This is estimated at around \$0.05/m^3 and is added directly to the overall operational cost.

3. Results

3.1. OMW Characterization

As mentioned above the OMW samples used in this study were obtained from an "olive oil mill located in Ajloun, Jordan". Table 2 presents the initial properties of OMW from the current research in comparison with findings from previous research.

As shown in Table 2, the wastewater samples collected from the olive oil mill exhibited significant variations in their characteristics, which can be attributed to the timing of sample collection during the olive harvest season. Each sampling period—early October and late December—coincided with different stages of olive processing, thereby influencing wastewater composition. Several parameters, such as the quantity and quality of olives processed, variations in extraction methods, and the natural degradation of organic materials over time, influence the differences in some parameters like pH, COD, BOD_5, and turbidity [59]. For instance, turbidity levels rose dramatically from 732 NTU in OMW I to 2656 NTU in OMW II, indicating a higher concentration of suspended solids later in the season. This increase can be linked to the accumulation of organic matter and phenolic compounds as the harvest progresses, which may lead to more pronounced environmental impacts. Thus, the timing of sample collection is crucial for understanding these variations and their potential ecological consequences. This finding aligns with the conclusions of Galanakis [59], which emphasized that the characteristics of OMW fluctuate based on seasonal factors, the timing of collection, and the specific extraction methods employed. Such insights highlight the need for careful consideration of sampling strategies in future studies to accurately assess the environmental implications of wastewater from olive oil production.

Table 2. Comparative initial properties of OMW from the current research and previous research.

Parameters	Unit	Current Study		[60]	[61]	[62]	[63]	[64]		[65]	[66]	
		OMW I	OMW II					Sample A	Sample B		1st Sample	2nd Sample
pH	-	4.54–4.65	5.2	4.6–5.1	4.2–5.5	4.62 ± 0.01	6.5	4.53 ± 0.02	4.47 ± 0.03	4.91	5.2	5.6
BOD_5	mg O_2/L	9000	32,000	5260	17,640–41,720	-	1050	22,500	28,400	36,329	8900	22,000
COD	mg O_2/L	55,800	191,100	25,800–146,000	45230–106,800	52,100	2500	100,800	118,500	58,614	180,000	121.000
BOD_5/COD	-	0.161	0.167	0.204–0.036	0.39–0.391	-	0.42	0.22 ± 0.03	0.24 ± 0.024	0.62	0.049	0.182
TKN	mg O2/L	396.5	453.8	-	-	-	-	-	-	544	-	-
TPh	g/L	5321	5830	1540	-	6920	-	8710	7420	2269	5500	4500
Turbidity	NTU	732	2656	1264	-	-	323	-	-	-	-	-
TS	mg/L	85,747	78,470	-	-	-	3400	-	-	-	91,200	72,000
TSS	mg/L	2289	1687	12,760	-	-	-	25,500	22,660	-	-	-

Overall, the low BOD_5/COD ratio observed in this study indicates notable differences in the composition of the organic part compared to previous studies. This highlights the significance of harvesting processes and the period of sample collection in assessing the environmental impact of OMW. The high concentration of non-biodegradable organic material in our findings suggests that more aggressive treatment methods may be necessary to mitigate potential environmental risks associated with OMW disposal.

3.2. Olive Stone Characterization

Based on our previous study [48], we found that the optimal pyrolysis temperature for producing biochar from OS was 500 °C. In this study, we examined the properties of biochar produced at this temperature over different pyrolysis durations: 1, 3, and 5 h. Table 3 provides a summary of the key properties and biochar surface area generated at a pyrolysis temperature of 500 °C.

Table 3. Surface characteristics and physicochemical properties of biochar generated at 500 °C.

Parameters	**Unit**	**Duration (h)**		
		1	**3**	**5**
Ash Contents	%	3.83	7.55	7.79
Yield	%	25.175	27.23	28.11
Moisture Contents	%	1.48	1.86	1.20
Electrical Conductivity	mS/cm	0.082	0.179	0.078
Surface Structure				
Langmuir Surface area	m^2/g	64.77	10.72	70.50
"Single point Surface area at P/Po = 0.297"	m^2/g	41.28	6.94	38.92
Total pore volume	cm^3/g	0.0055	0.025	0.026
Average pore width	Å	31.59	23.11	23.99
Zeta Potential	mV	−32.21	−27.08	−26.39
BET Surface area	m^2/g	6.99	43.63	44.19

Table 3 indicates that the analysis of the physicochemical properties and surface features of biochar generated at 500 °C is particularly relevant in relation to the duration of pyrolysis and its impact on wastewater treatment efficiency. The yield of biochar in our study increased from 25.175% at 1 h to 28.11% at 5 h, which is somewhat unexpected. Typically, higher pyrolysis temperatures lead to a loss of volatile compounds, resulting in lower yields [67] This trend contrasts with findings by Abid et al. [68], which reported yields of 32.08% at lower temperatures. The increase in yield in our study may suggest that extended pyrolysis stabilizes organic compounds within the biochar matrix, challenging established trends that indicate a decrease in yield with increased temperature.

The Langmuir surface area exhibits notable variability across the different pyrolysis durations. At 1 h, the surface area is measured at 64.77 m^2/g, indicating a relatively high surface area conducive to adsorption. However, this value decreases dramatically to 10.72 m^2/g at 3 h, suggesting a possible alteration in the structural integrity of the biochar during this period. Interestingly, the surface area rebounds to 70.50 m^2/g at 5 h, which may indicate a reorganization of the biochar structure that enhances its surface characteristics. Such fluctuations underscore the complex relationship between pyrolysis duration and surface morphology.

In terms of the single point surface area, the results reveal a significant drop from 41.28 m^2/g at 1 h to a mere 6.94 m^2/g at 3 h. This decrease raises concerns about the potential degradation of surface features that are critical for adsorption. Although the single point surface area recovers slightly to 38.92 m^2/g at 5 h, it does not reach the initial level, highlighting the need for caution in interpreting these findings. The observed changes may reflect the dynamic nature of biochar formation, where extended pyrolysis enhances certain structural characteristics while potentially compromising others.

Ash content showed a significant increase from 3.83% at 1 h to 7.79% at 5 h, which indicates enhanced mineral retention at elevated temperatures. Higher ash content can improve the adsorption capacity of biochar. Moisture content varied slightly, with values of 1.48% at 1 h, peaking at 1.86% at 3 h, and then decreasing to 1.20% at 5 h. This trend suggests that optimal moisture retention occurs at 3 h, enhancing contact with dissolved pollutants. The reduction at 5 h may indicate structural changes that could affect the biochar's ability to retain moisture, which is critical for its effectiveness in wastewater applications.

The total pore volume demonstrates a consistent increase from 0.0055 cm^3/g at 1 h to 0.026 cm^3/g at 5 h. This trend suggests that longer pyrolysis durations facilitate the development of additional pores, thereby enhancing the biochar's capacity for pollutant adsorption. Concurrently, the average pore width decreases from 31.59 Å at 1 h to 23.11 Å at 3 h, before stabilizing at 23.99 Å at 5 h. Such a shift indicates the formation of smaller, more numerous pores over time, which may contribute to improved adsorption properties. The BET surface area shows a sharp increase from 6.99 m^2/g at 1 h to 43.63 m^2/g at 3 h, stabilizing at 44.19 m^2/g at 5 h. This significant enhancement in surface area is indicative of the biochar's growing potential for pollutant interactions as pyrolysis duration increases, aligning with the observed increases in total pore volume.

The zeta potential values provide further insight into the stability and behavior of biochar in suspension, as shown Figure S1. At 1 h, the zeta potential is measured at -32.21 mV, indicating a moderately negative charge that promotes stability and prevents particle aggregation. As the pyrolysis duration increases to 5 h, the zeta potential decreases to -27.08 mV. This slight reduction suggests an enhancement in negative surface charge density, which is beneficial for preventing aggregation and facilitating interactions with dissolved pollutants. However, this change may also indicate alterations in surface characteristics that could impact the biochar's overall effectiveness in pollutant adsorption.

The X-ray diffraction (XRD) patterns illustrated in Figure 2 provide insights into the structural characteristics of biochar generated at 500 °C for varying pyrolysis durations and raw OS. For the biochar produced for 1 h, the XRD pattern reveals broad and low-intensity peaks, indicating a predominantly amorphous structure. The lack of well-defined peaks suggests minimal graphitization, which may limit the biochar's effectiveness in adsorption applications, as the amorphous carbon generally has a lower surface area and reactivity. In contrast, the biochar produced for 3 h shows sharper and more defined peaks, reflecting an increase in crystallinity. This transition suggests that longer pyrolysis durations facilitate the formation of a more ordered carbon structure, enhancing the material's stability and potentially improving its adsorption properties. The most pronounced changes are observed in the XRD pattern for biochar produced for 5 h, where the peaks are well-defined and exhibit the highest intensity among the four durations shown in Figure 2. This pattern indicates a significant increase in crystallinity and graphitization, suggesting that prolonged pyrolysis enhances the structural integrity of the biochar. The increased order within the carbon structure at this duration likely contributes to superior adsorption capabilities, making it more effective in removing contaminants from aqueous solutions.

The XRD pattern labeled as "raw OS," located at the bottom of Figure 2, reflects distinct characteristics compared to the biochar samples. This spectrum shows a relatively flat baseline with minimal peaks, suggesting that the OS may have a different composition or structural arrangement than the biochar samples. The lower intensity and lack of sharp peaks indicate a more amorphous or less crystalline structure, which may imply limited carbonization or a different material composition. This could have implications for its potential applications in adsorption or environmental remediation, as its structural properties are less favorable compared to those of the biochar produced at longer pyrolysis durations. Overall, as the pyrolysis duration increases, the crystallinity and structural order of the biochar improve significantly. This progression from an amorphous to a more ordered structure is critical for enhancing the biochar's performance in environmental applications, particularly in pollutant adsorption. The optimal structural properties appear to be achieved at around 5 h of pyrolysis.

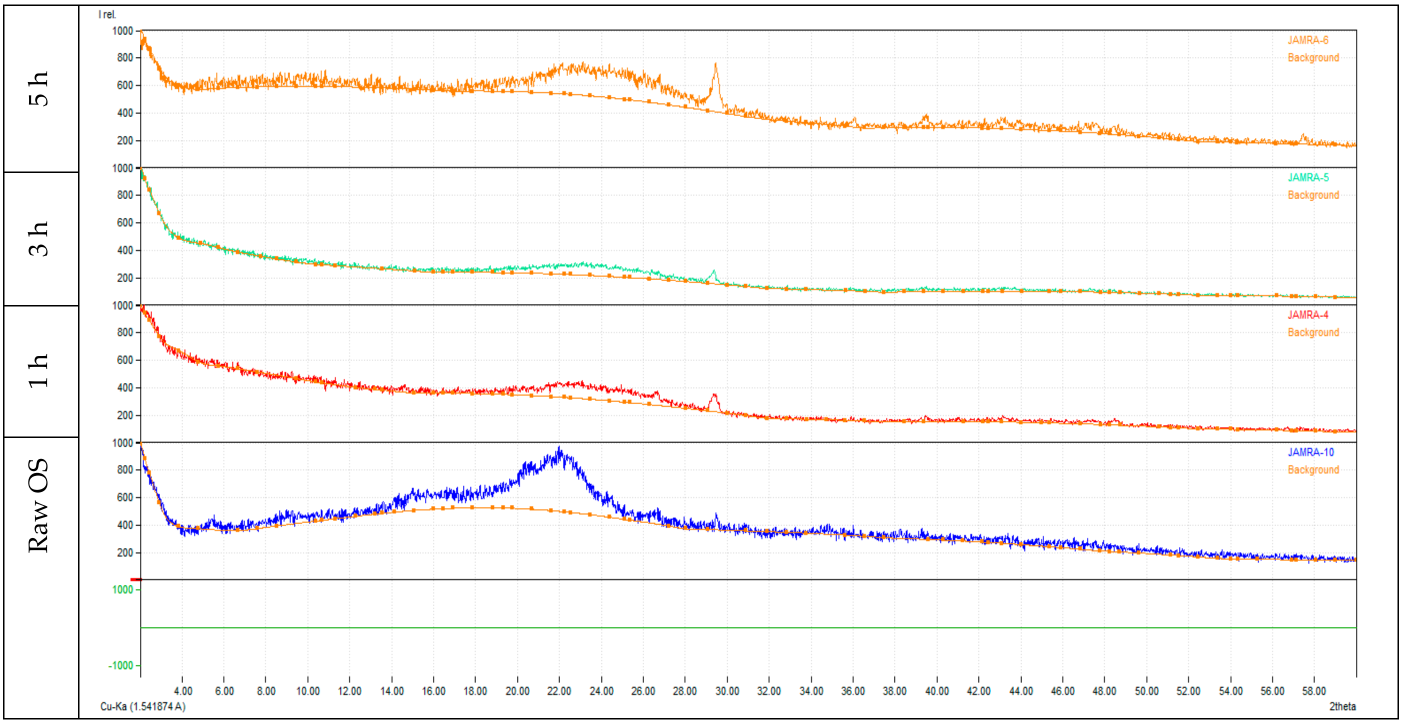

Figure 2. XRD Patterns of biochar produced at 500 °C for different pyrolysis durations (From top to bottom: 5, 3, 1 h, and raw OS).

The SEM micrographs presented in Figure 3 provide critical visual evidence that complements the quantitative findings discussed regarding the surface characteristics of biochar produced at varying pyrolysis durations, as shown in Table 3. Each image distinctly illustrates the morphological alterations that correlate with the changes in surface area and porosity metrics.

Figure 3a depicts untreated OS and serves as a control, establishing a baseline for the structural characteristics prior to pyrolysis. This comparison facilitates an understanding of the transformational processes that occur during pyrolysis. Figure 3b, representing biochar produced at a pyrolysis duration of 1 h, reveals a relatively rough and porous surface morphology. This observation aligns with the recorded Langmuir surface area of 64.77 m^2/g, suggesting that the initial stages of pyrolysis enhance the biochar's surface characteristics, thereby promoting adsorption potential. The presence of pronounced surface features is indicative of effective interaction sites for contaminants.

In contrast, Figure 3c, corresponding to the 3 h pyrolysis duration, exhibits a notable alteration in structure. The marked reduction in the single point surface area to 6.94 m^2/g is visually corroborated by a more compact and less porous morphology. This observation is consistent with the discussion regarding the potential degradation of surface features, which could adversely affect the adsorption capacity of the biochar. Figure 3d, representing biochar produced at 5 h, displays a more intricate and porous structure. This structural complexity aligns with the observed rebound in the Langmuir surface area to 70.50 m^2/g, indicating that prolonged pyrolysis facilitates a reorganization of the biochar framework, thereby enhancing its structural and functional characteristics. Based on the analysis of the SEM micrographs and quantitative data, a pyrolysis duration of 5 h is optimal for producing biochar.

Figure 3 shows the SEM micrographs of biochar pyrolyzed at 500 °C for different durations: (a) untreated OS and (b) 1 h, (c) 3 h, and (d) 5 h.

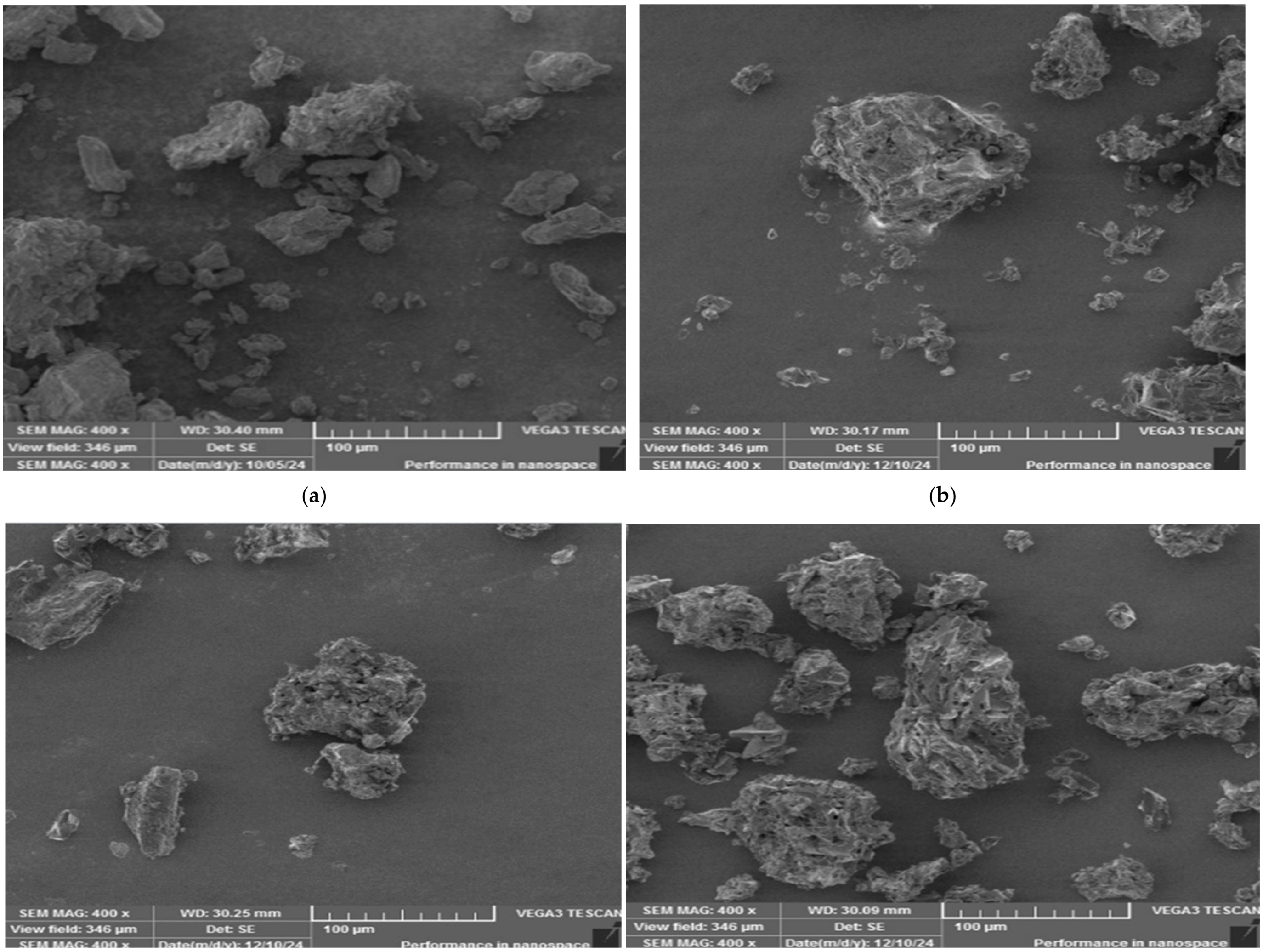

(**a**) (**b**)

(**c**) (**d**)

Figure 3. SEM micrographs of biochar pyrolyzed at 500 °C for different durations: (**a**) untreated OS and (**b**) 1 h, (**c**) 3 h, and (**d**) 5 h.

The following discussion provides an analysis of the FTIR spectra, elucidating the functional groups present in the raw OS and the biochar produced at varying pyrolysis durations, as shown Figure S2. The analysis of raw OS reveals significant findings, including a band at 421 cm^{-1} that indicates metal-ligand interactions, along with a C-O stretching band at 1040 cm^{-1}, confirming the presence of carboxylic acids and alcohols. Biochar produced at 500 °C for 1 h retains inorganic compounds, as evidenced by the band at 419 cm^{-1}, and features a C-O stretching band at 1244 cm^{-1}, which is essential for pollutant adsorption.

After 3 h of pyrolysis, the spectrum shows a C-O stretching band at 1233 cm^{-1}, indicating the presence of functional groups that enhance adsorption capabilities. The biochar generated after 5 h displays a C=C stretching band at 1644 cm^{-1}, crucial for its stability, alongside an O-H stretching band at 3286 cm^{-1}. This suggests the presence of phenolic groups that are important for interactions with water and nutrients.

Overall, the findings indicate that the 5 h pyrolysis treatment significantly enhances the biochar's stability and pollutant adsorption potential, making it particularly effective for wastewater treatment applications. This aligns with the findings reported by Abid et al. [68], ElHajjouji et al. [69], and Hafidi et al. [70], reinforcing the importance of extended pyrolysis in optimizing biochar properties for environmental applications.

3.3. Statistical Analysis

The runs were carried out effectively using a design matrix developed through the CCD method. Measurements of turbidity, TKN, TPh, COD_{total}, and $COD_{soluble}$ were conducted in accordance with the methodologies specified. The applied current and voltage recorded for each trial were used to compute the *ENC*, and $ELC_{theoretical}$, which served as an additional response variable. The weight of anodes measured for each trial were used to compute ELC_{actual}. RSM was applied to assess the impact of the variables and the corresponding regression equations.

ANOVA

The findings from the CCD analysis indicate a good fit by the quadratic model for the eight responses based on the "response surface regression analysis." The statistical analysis demonstrated that various parameters significantly impact the percentage removal of pollutants when using two Al electrodes.

The analysis revealed that increasing the CD, reaction time, and distance positively influences the percentage removal rates for COD_{total} and $COD_{soluble}$ (Equations S1 and S2). However, diminishing returns were noted at higher levels of these parameters, suggesting that beyond a certain point, further increases may not yield proportional benefits. For TPh, while increases in CD and time enhance pollutant removal, the distance showed a negative impact, indicating complex interactions among the variables (Equation S3). In the case of turbidity, higher CD values contributed positively to removal efficiency, while increased reaction time appeared to hinder it (Equation S4). The analysis of TKN highlighted the importance of balancing CD, time, and distance to optimize removal rates without exceeding efficient operational levels (Equation S5). Furthermore, the *ENC*, represented by both theoretical and actual $ELC_{theoretical}$ and ELC_{actual}, was found to increase with higher values of CD, time, and distance, emphasizing the need for careful management of these parameters to avoid excessive energy use (Equations S6–S8).

Overall, the statistical analysis underscores the need for careful optimization of parameters to enhance efficiency while managing energy costs and avoiding diminishing returns. The coefficients of determination (R^2) provided in Table 4 further elucidate the models' predictive power, indicating their effectiveness in explaining variability in percentage removal.

Table 4. The R^2, adjust R^2, and predicted adjusted R^2 values for all models.

Model	R^2	R^2_{adj}	R^2adj (Pred)
%COD_{total}	90.63	86.84	77.27
%$COD_{soluble}$	80.81	73.05	68.62
%TPh	95.87	94.20	91.63
%TKN	91.18	87.61	74.04
%Turbidity	42.03	28.14	84.02
ENC	87.59	82.56	66.89
$ELC_{(theoretical)}$	91.09	88.95	81.96
$ELC_{(actual)}$	35.73	20.33	0.00

As shown in Table 4, the R^2, adjusted R^2, and predicted adjusted R^2 values offer valuable insights into the effectiveness of the models evaluating pollutant percentage removal and *ENC*, $ELC_{theoretical}$, and ELC_{actual} metrics. The COD_{total} model achieves a high R^2 of 90.63% and an adjusted R^2 of 86.84%, indicating that it explains a portion of the variability in COD removal. The TPh model exhibits even stronger performance, with an R^2 of 95.87% and an adjusted R^2 of 94.20%, reflecting robust explanatory power. In contrast, the $COD_{soluble}$ model presents an R^2 of 80.81% and an adjusted R^2 of 73.05%, which is still adequate but indicates some limitations in its explanatory strength [71]. The TKN model also performs well, with an R^2 of 91.18% and an adjusted R^2 of 87.61%. However, the turbidity model shows more limited explanatory power, with an R^2 of 42.03% and an adjusted R^2 of 28.14%, suggesting a need for refinement. the *ENC* model has an R^2 of 87.59% and an adjusted R^2 of 82.56%, indicating moderate explanatory capability but highlighting areas for potential enhancement. $ELC_{theoretical}$ model shows strong performance with an R^2 of 91.09% and an adjusted R^2 of 88.95%, indicating high reliability in predicting pollutant density. Lastly, the ELC_{actual} model has a low R^2 of 35.73% and an adjusted R^2 of 20.33%, suggesting significant limitations and the need for improvement to better reflect real-world conditions. Figure 4a–c, compare the experimental with the predicted results for the percentage removal of the TPh, TKN, and COD_{total} models, respectively.

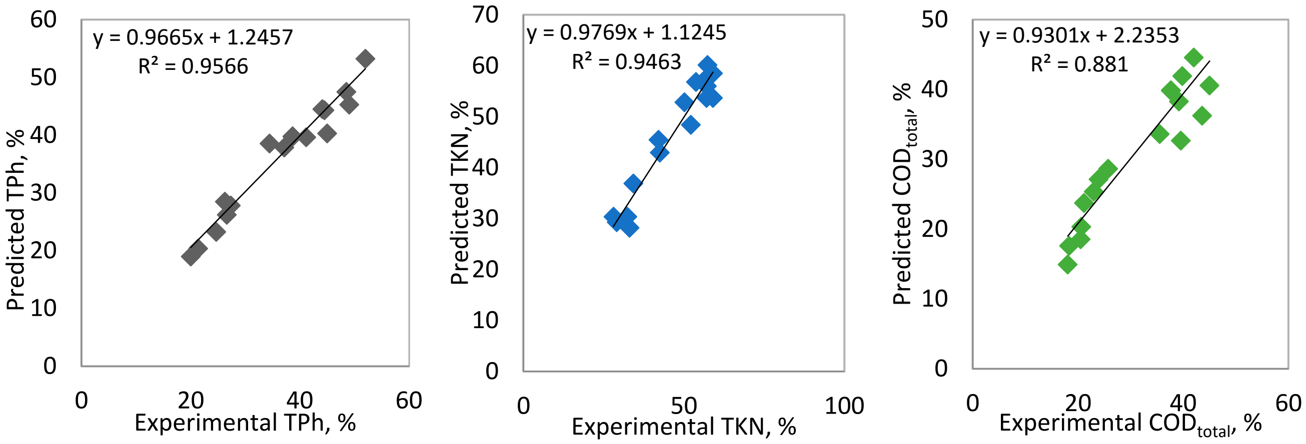

(**a**) (**b**) (**c**)

Figure 4. Comparison of predicted and experimental results for: (**a**) TPh, (**b**) TKN, and (**c**) COD_{total}.

As shown in Figure 4a–c, the data points align significantly with the diagonal lines, indicating a good correlation between predicted and experimental results. The R^2 values further substantiate these findings, with TPh achieving an R^2 of 95.66% and TKN reaching 94.63%. Although COD_{total} has an R^2 of 88.1%, which is below 90%, it still reflects a meaningful relationship between the predicted and experimental results, as noted by Hamid et al. [55]. This emphasizes the model's reliability in predicting percentage removal, particularly for TPh and TKN.

The coefficient t values of all models are summarized in Table 5. Table 5 shows the assessment of each term's significance in the model, which is conducted using the F-value, where a higher F-value reflects a greater level of significance [54]. "The *p*-value", particularly when it is less than 0.05, serves as an important benchmark for evaluating the adequacy of the F-value." "This indicates whether the model's significance is sufficient at a 95% confidence level."

Table 5. ANOVA for the TKN, Turbidity, TPh, COD_{total}, and $COD_{soluble}$ models (× is a multiplication sign).

Term	F-Value	COD_{total}		F-Value	$COD_{soluble}$		F-Value	TPh		F-Value	Turbidity		F-Value	TKN	
		t-Value	*p*-Value		t-Value	*p*-Value		t-Value	*p*-Value		t-Value	*p*-Value		t-Value	*p*-Value
Model	23.91	-	0.000	10.41	-	0.000	57.34	-	0.000	0.92	-	0.555	25.54	-	0.000
Linear	28.27	-	0.000	12.37	-	0.000	79.16	-	0.000	1.30	-	0.284	15.11	-	0.000
T	46.38	6.81	0.000	41.14	81.72	0.000	269.54	16.42	0.000	2.28	1.51	0.139	42.50	6.52	0.000
CD	35.78	5.98	0.000	8.96	16.42	0.001	11.77	3.43	0.001	1.04	−1.02	0.313	1.41	−1.19	0.241
D	4.16	−2.04	0.048	0.87	3.43	0.004	9.53	−3.09	0.004	0.68	−0.83	0.413	7.77	−2.79	0.008
N	21.61	−6.38	0.000	3.20	−6.34	0.000	30.99	−6.34	0.000	0.87	−1.27	0.428	5.81	−3.32	0.006
Square	36.75	-	-	9.19	-	-	45.22	-	-	0.86	-	0.470	59.04	-	0.000
T × T	61.84	−7.86	0.000	25.53	−10.21	0.000	104.17	−10.21	0.000	0.92	0.96	0.342	89.22	−9.45	0.000
CD × CD	9.47	−3.08	0.004	0.13	−1.70	0.097	2.89	−1.70	0.097	1.82	−1.35	0.184	28.53	−5.34	0.000
D × D	3.15	−1.77	0.083	0.09	3.31	0.002	10.99	3.31	0.002	0.04	−0.20	0.845	0.14	−0.37	0.710
Interaction	3.07	-	-	0.81	-	-	0.93	-	-	0.91	-	0.526	2.10	-	0.052
T × CD	12.36	3.52	0.001	0.41	1.70	0.097	2.89	1.70	0.097	1.45	1.20	0.235	6.65	−2.58	0.013
T × D	1.34	−1.16	0.253	0.28	−0.31	0.755	0.10	−0.31	0.755	0.49	0.70	0.490	3.11	−1.76	0.085
T × N	7.32	−3.61	0.002	2.27	−1.01	0.320	1.19	−1.01	0.320	0.35	−0.74	0.708	1.09	−0.49	0.347
CD × D	0.05	−0.23	0.820	1.47	−0.44	0.662	0.19	−0.44	0.662	3.78	−1.95	0.056	0.77	−0.88	0.385
CD × N	0.40	−0.19	0.676	0.15	0.09	0.926	0.03	0.09	0.926	0.70	−0.90	0.504	1.64	−1.78	0.207
D × N	0.05	0.17	0.952	0.14	−1.54	0.132	1.48	−1.54	0.132	0.02	−0.15	0.979	1.34	0.53	0.274
Lack of Fit	1.87	-	0.126	0.71	−0.12	-	-	-	-	1686.83	-	0.000	-	-	-

Table 5 presents the ANOVA outcomes for the COD_{total}, $COD_{soluble}$, TPh, turbidity, and TKN models. For COD_{total}, the overall model is highly significant with an F-value of 23.91 and a *p*-value of 0.000. Key linear terms, including "Time (T)" and "Current Density (CD)," both show strong positive effects, while "Distance (D)" and "Number of Electrode (N)", are also significant. Squared terms (T^2) and (CD^2) are significant, and the interaction "Time and CD (T × CD)" shows significance as well. The model fits the data well, indicated by a lack of fit *p*-value of 0.126. In $COD_{soluble}$, the model is significant with an F-value of 10.41 and a *p*-value of 0.000.

Significant linear terms include "T" and "CD," with strong effects, while "Distance (D)" and "N" also contribute significantly. The squared term (T^2) is significant, but (CD^2) is not. Interaction terms show limited significance. For TPh, the model demonstrates a strong overall significance with an F-value of 57.34 and a *p*-value of 0.000. Linear terms, particularly "T" and "N," are highly significant, and (T^2) shows a strong quadratic effect. Interaction terms have varying significance, with some being marginally significant. The turbidity model is not significant, with an F-value of 0.92 and a *p*-value of 0.555, indicating no significant effects from the tested parameters. In contrast, TKN shows a significant model with an F-value of 25.54 and a *p*-value of 0.000. Key terms like "T" and "CD" have strong effects, along with significant contributions from "D" and "N." Finally, the ENC model is also significant, with an F-value of 17.43 and a *p*-value of 0.000, showing important effects from linear terms and some significant interactions. Overall, while turbidity lacks significant relationships, TKN demonstrates strong influences from operational parameters, confirming the effectiveness of the models in capturing percentage removal.

"The Pareto chart," along with the major impacts of each variable on pollutant percent removal, is illustrated in Figure 5. For COD_{total} (Figure 5a), the term "AA" is the most significant, showing a high effect around 8. Other important terms include "A," "D," and "B," each contributing positively but to a lesser extent. The dashed line at 2.018 indicates the significance threshold; terms above this line are influential, highlighting key factors for optimizing COD percentage removal. In the $COD_{soluble}$ chart (Figure 5b), the term "A" stands out as the most significant factor, with a standardized effect around 6. Following "A," terms such as "AA," "B," and "D" also demonstrate substantial positive effects. The influence of terms like "AD," "BC," and "C" decreases, while terms at the bottom show minimal impact. The significance threshold is again indicated by the dashed line at 2.018.

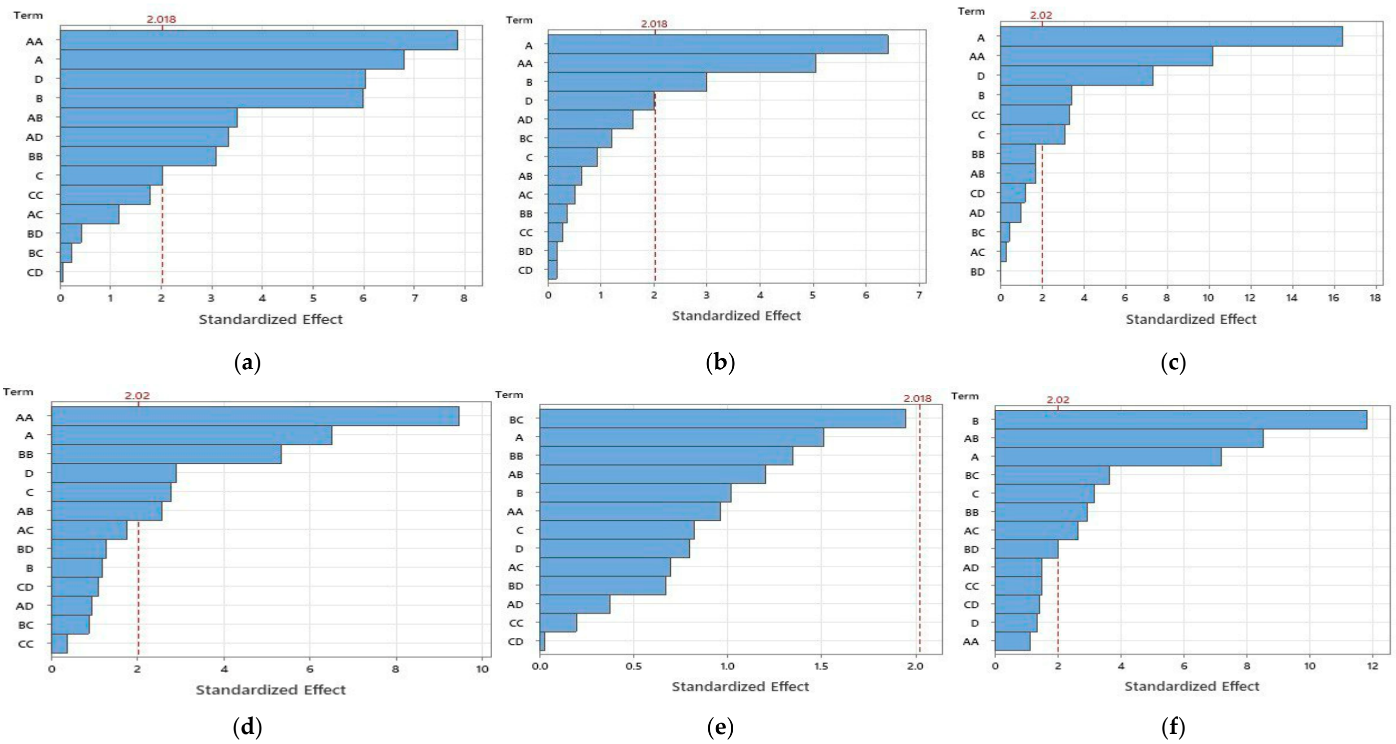

(**a**) (**b**) (**c**)

(**d**) (**e**) (**f**)

Figure 5. Pareto chart of standardized impacts on pollutant percentage removal (A: time, B: CD, C: distance, and D: number of electrodes). (**a**) COD_{total} (**b**) $COD_{soluble}$ (**c**) TPh (**d**) TKN (**e**) Turbidity (**f**) ENC.

For TPh (Figure 5c), the term "A" is the most significant, exhibiting a remarkably high standardized effect of around 16. Significant contributions also come from "AA," "D," and "B," while terms like "CC" and "C" have moderate effects. The dashed line at 2.02 marks the significance threshold, emphasizing the influential terms. In the TKN chart (Figure 5d), "AA" emerges as the most significant factor with a high standardized effect of around 10. The term "A" also shows a notable impact, while "BB," "D," and "C" contribute positively but to a lesser extent. The influence of terms such as "AB," "AC," and others diminishes further down the chart, with the significance threshold marked at 2.02. The turbidity chart (Figure 5e) highlights "BC" as the most significant factor, with a standardized effect close to 2. "A" also demonstrates a notable effect, while terms like "BB," "AB," and "AA" contribute positively. The influence of terms such as "D," "AC," and others declines, with the significance threshold at 2.018. Lastly, the *ENC* chart (Figure 5f) shows "B" as the most significant factor, exhibiting a high standardized effect of around 12. Following "B," terms "AB" and "A" also show substantial positive effects, while "BC," "C," and "BB" contribute moderately. The influence of terms like "AC," "BD," and others diminishes further down the chart, with the significance threshold indicated at 2.02.

The coefficient t values of *ENC*, $ELC_{theoritical}$, and ELC_{actual} model are summarized in Table 6.

Table 6 presents the ANOVA results for the *ENC*, $ELC_{theoretical}$, and ELC_{actual} models. For the *ENC* model, the overall model is significant with an F-value of 17.43 and a *p*-value of 0.000. Key linear terms, including T and CD, show strong positive effects, while D and N also contribute significantly. Interaction terms like T × CD are significant, indicating that the effects of T and CD are interconnected. In the $ELC_{theoretical}$ model, the overall significance is confirmed with an F-value of 21.56 and a *p*-value of 0.000. Significant linear terms include T and CD, with D and N also showing effects. The squared terms (T^2 and CD^2) are significant, suggesting non-linear influences. Interaction effects, particularly T × N, are noteworthy, highlighting the complexity of the electrode consumption dynamics. For ELC_{actual}, the model demonstrates strong significance with an F-value of 28.67 and a *p*-value of 0.000. Linear terms such as T and CD remain significant, while D and N also contribute meaningfully. The squared term (T^2) is significant, indicating a quadratic relationship, but (CD^2) does not show significance. Interaction terms display varying significance, particularly D × N, emphasizing the interactions between the number of electrodes and distance. Overall, all three models indicate significant relationships among the operational parameters, with varying degrees of interaction and non-linearity influencing energy and electrode consumption.

Table 6. ANOVA for the *ENC*, $ELC_{\text{theoritical}}$, and ELC_{actual} models.

Term	**F-Value**	***ENC***		**F-Value**	$ELC_{\text{theoretical}}$		**F-Value**	ELC_{actual}	
		t-Value	***p*-Value**		**t-Value**	***p*-Value**		**t-Value**	***p*-Value**
Model	17.43	-	0.000	42.67	-	0.000	2.32	-	0.002
Linear	39.03	-	0.000	113.61	-	0.000	5.2	-	0.000
T	51.52	7.18	0.000	298.2	17.27	0.000	15.32	3.91	0.000
CD	139.89	11.83	0.000	241.12	15.53	0.000	1.96	1.40	0.165
D	10.07	3.17	0.003	0.73	0.86	0.394	0.00	0.02	0.985
N	1.74	1.67	0.187	0.31	0.52	0.602	3.78	−1.76	0.026
Square	5.28	-	0.004	0.63	-	-	2.89	-	0.039
T × T	1.31	−1.15	0.259	0.04	0.19	0.849	7.73	2.78	0.007
CD × CD	8.74	2.96	0.005	0.30	−0.55	0.584	2.56	−1.6	0.113
D × D	2.22	1.49	0.144	0.84	−0.92	0.362	0.00	−0.04	0.965
Interaction	11.61	-	0.000	13.19	-	-	1.63	-	0.085
T × CD	72.96	8.54	0.000	101.6	10.08	0.000	0.63	0.79	0.431
T × D	6.98	2.64	0.012	2.62	1.62	0.109	0.02	−0.13	0.897
T × N	2.07	1.93	0.139	1.6	0.85	0.207	6.17	−1.84	0.003
CD × D	13.27	3.64	0.001	2.85	1.69	0.095	0.01	0.10	0.921
CD × N	3.23	2.51	0.049	2.19	1.09	0.118	0.02	−0.16	0.984
D × N	1.90	−0.61	0.163	1.81	−0.79	0.170	0.14	−0.39	0.872
Lack of Fit	1.82	-	0.003	-	-	-	1.29	-	0.000

3.4. Influence of Variables

3.4.1. Influence of Pollutant

Influence of COD_{total} and COD_{soluble}

To understand the interactions between independent variables and estimate COD_{total} and COD_{soluble} percentage removal, 3D response surface plots were constructed from regression equations. These plots show the influence of two selected variables on the percentage removal are held constant. Figure 6a–d provides a deep analysis of how the different parameters affect the percentage removal of COD_{total} and COD_{soluble}.

In Figure 6a, the interaction between CD and reaction time on COD_{total} percentage removal is illustrated. The figure indicates a nonlinear correlation, suggesting that as reaction time increases, the efficiency of COD_{total} removal improves until it achieved optimal levels. Specifically, maximum removal occurs within the ranges of 50–60 min for reaction time and 15–20 mA/cm^2 for CD. This observation aligns with findings from previous studies [72,73], which indicate that higher CDs enhance the hydrolysis of Al ions, resulting in increased sludge production and improved COD percentage removal. This enhancement can be attributed to the continuous formation of aluminum hydroxide ($Al(OH)_3$) flocs, which act as adsorbents for COD_{total} pollutants. Freshly generated flocs provide a larger surface area, facilitating greater adsorption of contaminants. In addition to the removal of COD_{total}, the EC process facilitates the separation of organic matter from the wastewater. During electrolysis, coagulated particles become trapped within the $Al(OH)_3$ flocs, forming larger aggregates. These aggregates, aided by the gas bubbles (H_2 or O_2) generated at the electrodes, rise to the surface, promoting effective separation [60,72]. This mechanism not only improves the overall COD_{total} removal but also enhances the efficiency of the treatment process, thereby contributing to the effectiveness of OMW management.

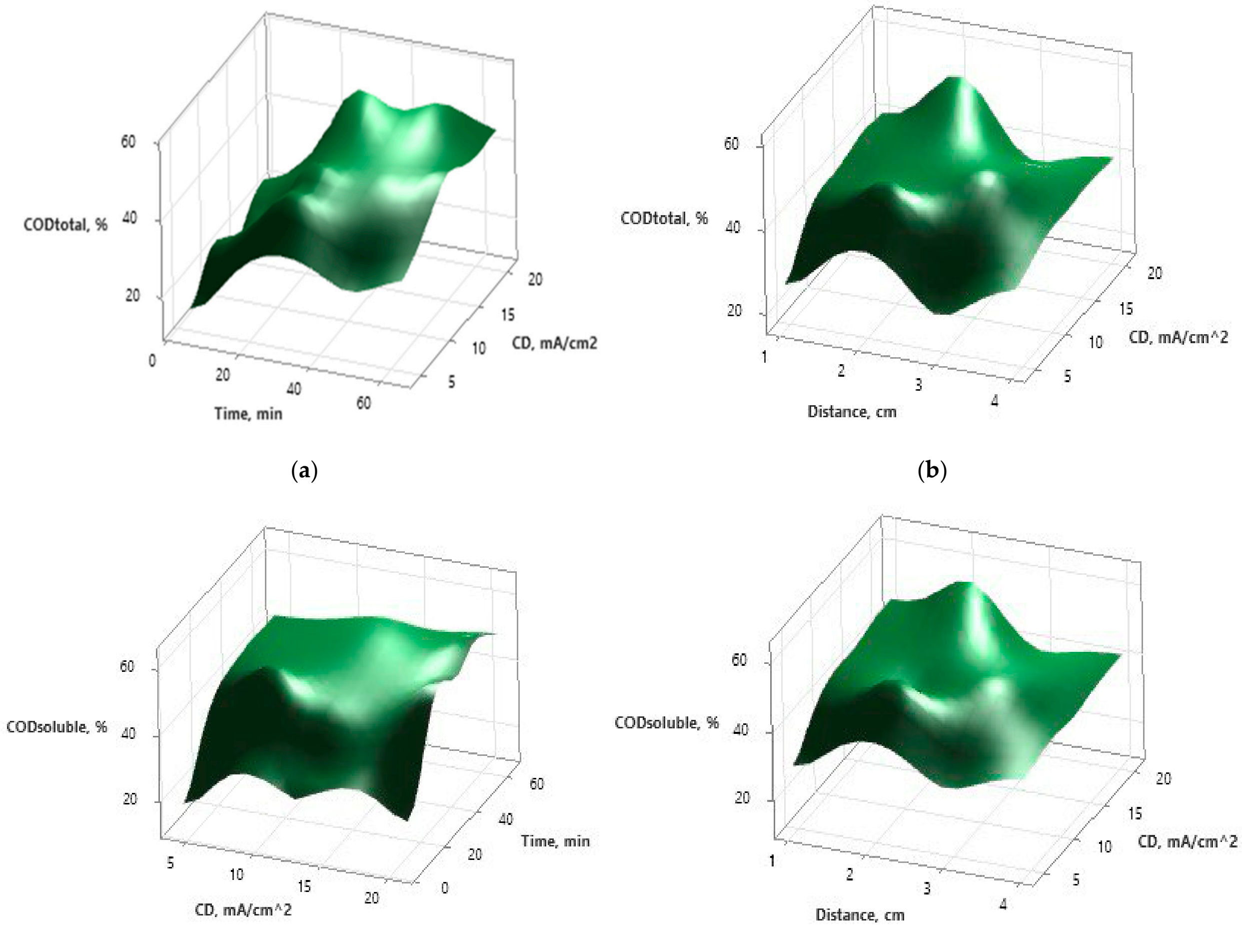

(**a**) (**b**)

(**c**) (**d**)

Figure 6. Influence of (**a**) time and CD on COD_{total}, (**b**) electrode spacing and CD on COD_{total}, (**c**) CD and time on $COD_{soluble}$, and (**d**) CD and electrode spacing on $COD_{soluble}$ percentage removal.

Figure 6b examines the effect of the electrode spacing on COD_{total} percentage removal while varying CD. The optimal distance for achieving maximum COD_{total} removal is approximately 1 cm. This result indicates that maintaining appropriate electrode spacing improves electric field strength, thereby enhancing ion movement and interaction, which are crucial for effective electrochemical processes. Prior research emphasizes the significance of electrode distance in optimizing treatment efficiency, with optimal distances facilitating better ion interactions and reaction rates [24,72,74]. Furthermore, previous research [75] highlights negative effects associated with reducing the electrode distance. Specifically, decreasing the spacing can lead to increased energy consumption without significant improvements in pollutant removal efficiency. This inefficiency arises because closer spacing can weaken the electric field strength, which adversely affects ion kinetics and overall reaction rates.

In Figure 6c, trends similar to those in Figure 6a are observed for $COD_{soluble}$ removal. The plot demonstrates that optimal $COD_{soluble}$ percentage removal is attained at higher levels of reaction time and CD, further emphasizing the significance of these parameters in enhancing percentage removal. Extended treatment times allow for more effective degradation of soluble organic contaminants, corroborating earlier findings [73,76,77]. Figure 6d provides insights into the relationship between electrode spacing and CD on $COD_{soluble}$

percentage removal. Similar to the previous figures, optimal $COD_{soluble}$ removal occurs when the electrode spacing is around 1 cm. This consistency across figures emphasizes the critical role of electrode spacing in maximizing treatment effectiveness, as insufficient spacing can lead to decreased efficiency due to weakened electric fields [74,78].

Overall, the analysis of these figures underscores the complex interactions among CD, time, and electrode spacing that collectively influence both COD_{total} and $COD_{soluble}$ percentage removal. Optimizing these parameters is essential for improving the effectiveness of EC.

Influence on Turbidity

Figure 7 presents 3D surface plots illustrating the impacts of CD, electrode spacing, and time on turbidity percentage removal. The discussion on these plots provides insights into optimizing turbidity removal in EC processes.

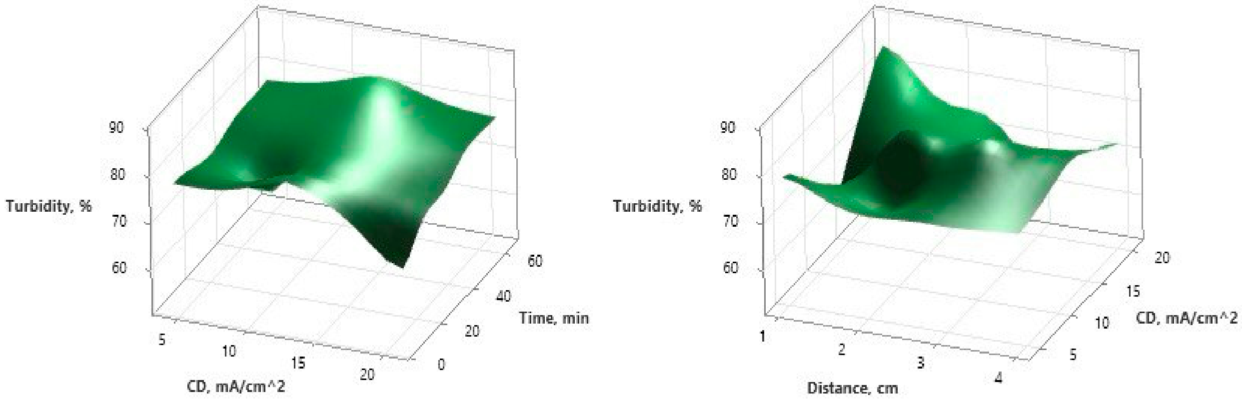

(**a**) (**b**)

Figure 7. Influence of (**a**) CD and time, and (**b**) CD and electrode spacing on turbidity percentage removal.

In Figure 7a, the highest turbidity percentage removal is achieved at extended reaction times, particularly when the CD is maintained between 10 and 15 mA/cm^2. Under these optimal conditions, with a time of 60 min, turbidity percentage removal exceeds 82.5%. The percentage removal increases steadily until it reaches a peak, after which it begins to decline at higher CDs. This trend indicates that while enhanced electrochemical reactions at optimal CDs enhanced solid aggregation, excessively high currents may lead to side reactions that hinder overall efficiency [79]. The initial sharp rise in turbidity percentage removal during the first 30 min indicates that the majority of turbidity reduction occurs in the early stages of the EC process, underscoring the importance of timely intervention in EC treatment [79].

Figure 7b depicts the effect of CD and electrode spacing on turbidity percentage removal. The plot shows that turbidity percentage removal decreases as the distance between electrodes increases. This finding indicates that closer electrode spacing enhances removal effectiveness. Optimal turbidity removal is achieved at minimal electrode distances, with efficiencies exceeding 85% at CDs around 10 to 15 mA/cm^2. The decline in efficiency at larger distances is referred to as increased resistance to mass transfer and reduced interaction between electrodes and reactants, both of which are critical for effective electrochemical reactions. As noted, increasing the electrode distance can hinder performance, confirming that maintaining closer spacing is vital for maximizing turbidity percentage removal.

Overall, the findings from Figure 7a,b emphasize the importance of both electrode spacing and reaction time in optimizing turbidity percentage removal. The results indicate that maintaining an optimal current density and minimizing electrode distance are crucial for achieving high percentage removal in electrochemical processes.

Influence on TPh and TKN

Figure 8 showcases 3D surface plots that analyze the influence of CD, distance between electrodes, and time on the percentage removal of TPh and TKN. This analysis reveals important relationships among these parameters. In Figure 8a, TPh percentage removal shows a marked increase with prolonged reaction times, reaching a peak efficiency of approximately 55–58% in 50 to 60 min. This indicates the critical role of adequate time for efficient removal. Although higher CDs also enhance TPh removal, their effect is less substantial compared with that of time. This indicates that the reaction time is paramount for achieving the maximum efficiency, particularly due to the challenges posed by the polymerization and autooxidation of polyphenolic chemical during storage [80,81].

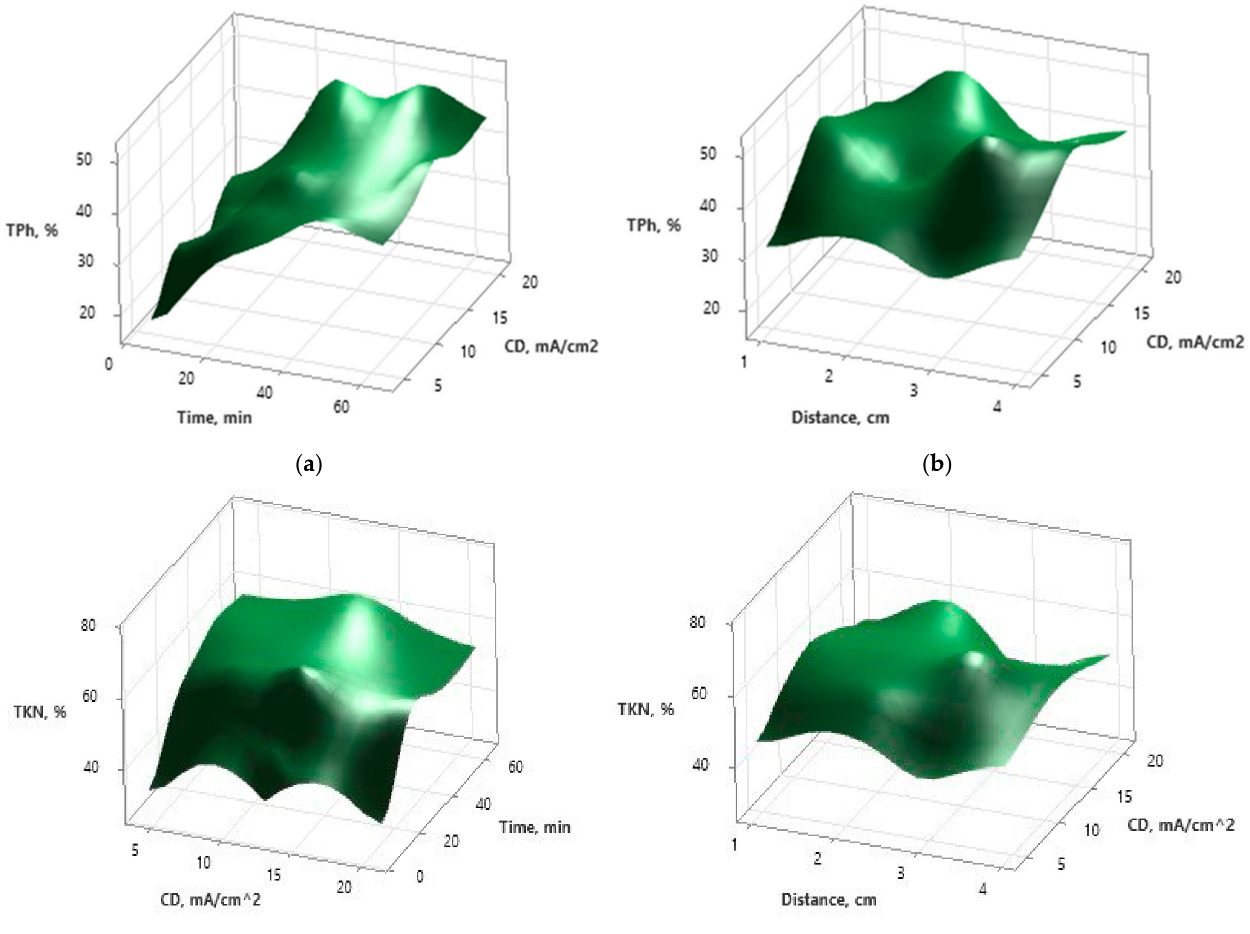

(**a**) (**b**) (**c**) (**d**)

Figure 8. Influence of (**a**) CD and time on TPh, (**b**) CD and electrode spacing on TPh, (**c**) CD and time on TKN, and (**d**) CD and electrode spacing on TKN percentage removal.

However, it is important to recognize that beyond a certain reaction time, the efficiency of TPh removal may plateau or even decline. This phenomenon can be explained by the saturation of available surface area on the flocs. When flocs become saturated, their capacity to adsorb additional phenolic compounds diminishes, which can lead to reduced effectiveness in the removal process. Furthermore, prolonged reaction times can destabilize the flocs, causing them to break apart and lose their ability to effectively capture TPh.

Figure 8b illustrates that optimal TPh removal occurs at an electrode spacing of approximately 1 cm. At this spacing, percentage removal is maximized, while intermediate distances of 2 and 3 cm show reduced effectiveness. Interestingly, TPh percentage removal increases again at a distance of 4 cm, indicating that there may be an optimal range for electrode spacing. This variation implies that the efficiency of TPh removal is not consistent across distance and may depend on how CDs is distributed.

Moving to Figure 8c, TKN percentage removal increases with extended reaction time, peaking at 70% after approximately 40 min. Additionally, TKN removal improves progressively with rising CD, achieving optimal efficiency at around 17 mA/cm^2. This indicates that both extended reaction time and optimal CD are crucial for maximizing TKN removal. The observed trend reflects the enhanced EC reactions driven by higher CDs, facilitating effective reduction and oxidation methods. Figure 8d indicates that TKN percentage removal declines as the electrode spacing increases, with the highest efficiency noted at the shortest distance of 1 cm. The efficiency significantly rises at 2 cm, reaching about 60%, likely due to better mass transfer. However, at distances exceeding 2 cm, the efficiency begins to decrease.

Overall, the findings from Figure 8a–d highlight the importance of both electrode distance and time in enhancing the percentage removal of TPh and TKN. Reaction time emerged as a particularly critical factor for achieving high percentage removal, while optimal CD and appropriate electrode spacing also significantly influenced the outcomes.

3.4.2. Influence on Energy and Electrode Consumption

Influence on ENC

The 3D surface plots displayed in Figure 9 illustrate the relationships among CD, time, and electrode spacing on *ENC* during the EC process.

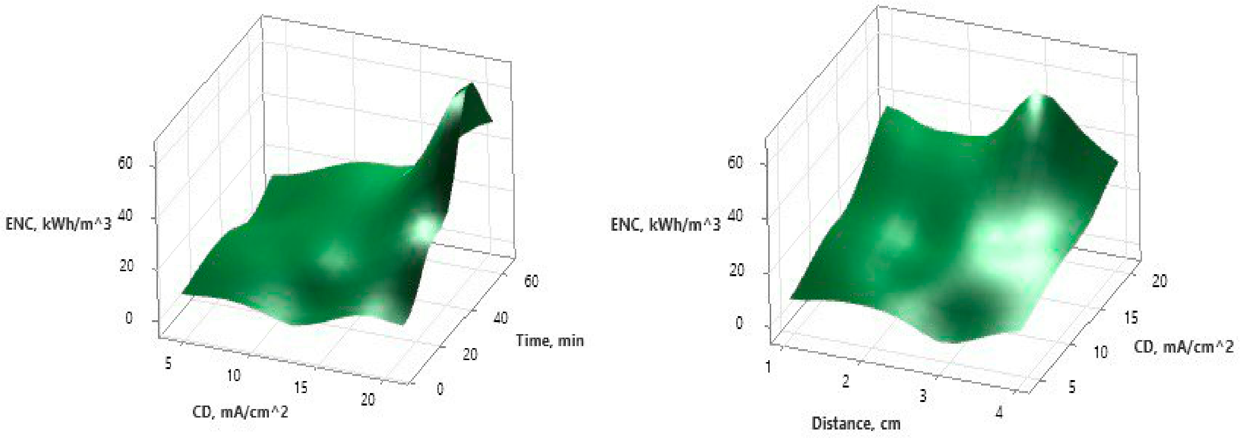

(**a**) (**b**)

Figure 9. Influence of (**a**) CD and time, and (**b**) CD and electrode spacing on *ENC*.

In Figure 9a, the analysis indicates a significant increase in *ENC* with both reaction time and CD, peaking at 60 kWh/m^3. This increase suggests that longer reaction times and higher CDs require more energy, likely due to the enhanced power required for ion movement and reaction facilitation. The *ENC* reaches its maximum of 60 kWh/m^3 when the CD was 20 mA/cm^2 and the time was 60 min. This change is associated with the increased energy demands for ion motion at high CD values [82]. Conversely, at lower values, such as 5 mA/cm^2 and 5 min, the *ENC* is measured at a more efficient 10 kWh/m^3.

Figure 9b illustrates that *ENC* also escalates with increased electrode distance. This trend can be explained by the need for more energy to maintain electrical conductivity and ion transfer over greater distances. As the inter electrodes distance increases, the in the electrolyte resistance increases, which means higher voltages are needed to achieve the high current. Consequently, this heightened resistance contributes to an increase in *ENC* [8]. This behavior contrasts with other response variables where percentage removal typically decreases as electrode spacing increases.

Influence on $\mathrm{ELC}_{\mathrm{actual}}$ and $\mathrm{ELC}_{\mathrm{theoretical}}$

Figure 10a illustrates the relationship between current density, reaction time, and ELC_{actual} in the treatment of OMW. Figure 10a shows a linear relationship where increased CD leads to reduced consumption of the anode. As CD rises, the anodic dissolution of Al occurs more efficiently, resulting in lower weight loss of the anode. This phenomenon is attributed to the rapid generation of Al ions at higher CDs, enhancing the EC process [57,60]. Conversely, as reaction time increases, the consumption of the anode also increases. Extended reaction times allow for greater interaction between the Al electrodes and the wastewater, leading to the formation of more $\mathrm{Al(OH)_3}$ necessary for effective coagulation. This aligns with findings that the extent of anodic dissolution increases with longer treatment times [57,83,84]. Figure 10b illustrates the relationship between the distance between electrodes and ELC_{actual} at varying CDs in the treatment of OMW.

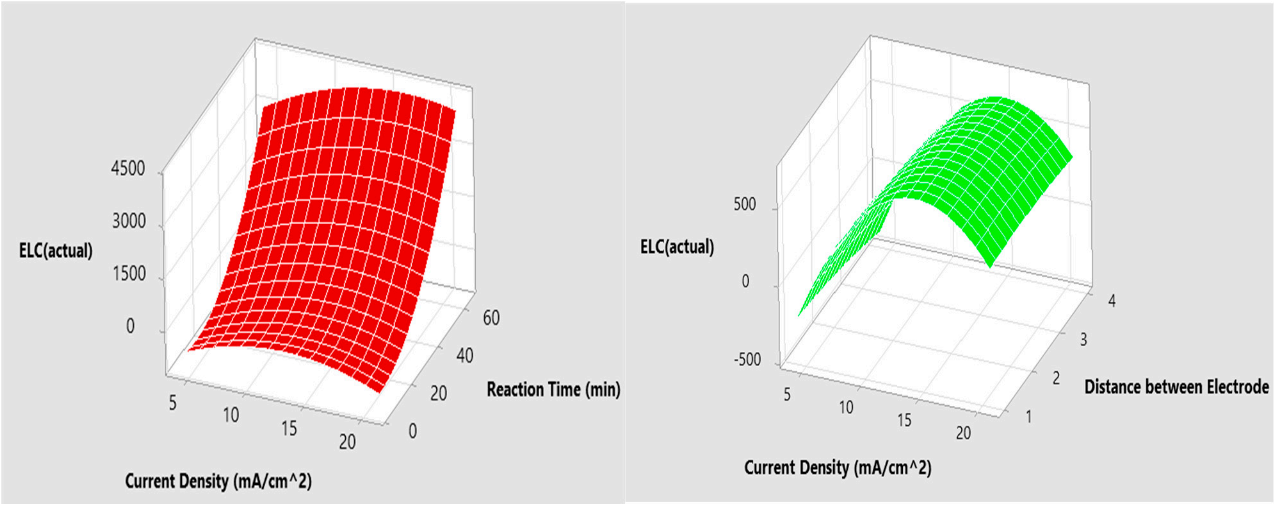

(**a**) (**b**)

Figure 10. Influence of (**a**) CD and time, and (**b**) CD and electrode spacing on ELC_{actual}.

Figure 10b highlights that while there is some variation in ELC_{actual} with changes in distance, the overall impact is minimal. This suggests that the electrocoagulation process is relatively robust against variations in electrode spacing within the examined distances, allowing for effective treatment of OMW without significant losses in electrode efficiency.

In Figure 11a, the relationship between $ELC_{\mathrm{theoretical}}$, CD, and reaction time is illustrated. The results indicate that while there is a measurable effect of current density on $ELC_{\mathrm{theoretical}}$, this effect is relatively limited compared to the influence of reaction time. As the reaction time increases, the $ELC_{\mathrm{theoretical}}$ rises significantly, reaching a maximum value of 1900 $\mathrm{g/m^3}$ at 65 min. This finding suggests that longer reaction durations enhance the effectiveness of the EC process, allowing for greater interaction between $\mathrm{Al^{3+}}$ ions and the pollutants in the wastewater. The increased reaction time facilitates better particle collision and floc development, which are critical for effective contaminant removal. This aligns with previous studies that have shown how prolonged electrolysis can lead to improved coagulation efficiency [60].

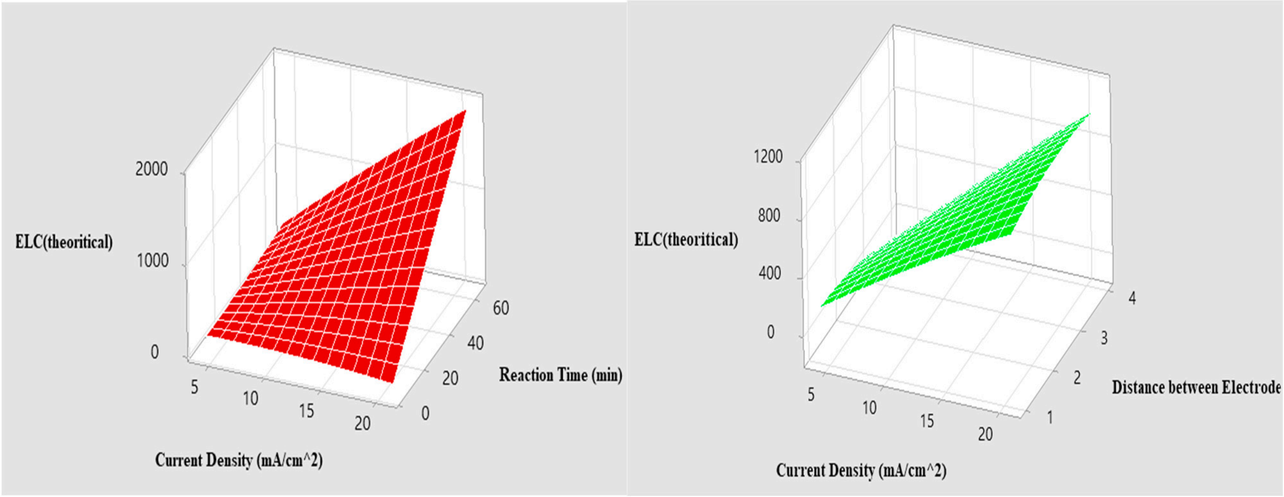

(**a**) (**b**)

Figure 11. Influence of (**a**) CD and time, and (**b**) CD and electrode spacing on $ELC_{theoretical}$.

Figure 11b presents the relationship between $ELC_{\text{theoretical}}$, CD, and the distance between electrodes. The data clearly indicate a significant impact of CD on $ELC_{\text{theoretical}}$. As the CD increases, there is a corresponding increase in $ELC_{\text{theoretical}}$. This relationship underscores the importance of CD in determining the rate of coagulant dosing, bubble formation, and overall fluid dynamics within the reactor, which ultimately affects particle collision and floc development.

However, the effect of distance between electrodes on $ELC_{\text{theoretical}}$ is minimal. This suggests that within the tested range, variations in electrode spacing do not significantly hinder the efficiency of Al^{3+} ion production and consumption. Therefore, optimizing CD remains the primary focus for enhancing the EC process.

3.4.3. Optimization the Operating Conditions for Al Electrodes and Energy Estimation

Optimization of responses can be effectively achieved through the use of Minitab 22.2 software, which enables systematic adjustments of parameters to achieve desired outcomes. In this process, responses can be set to maximize, minimize, or target specific values. In this research, the goal is to minimize the *ENC*, ELC_{actual}, $ELC_{\text{theoretical}}$ response while maximizing the percentage removal of COD_{total}, COD_{soluble}, TPh, and TKN. In our previous study [48], the parameters ELC_{actual} and $ELC_{\text{theoretical}}$ were not included in the process optimization. However, these parameters have been incorporated into our current study to enhance accuracy and improve treatment effectiveness.

The optimized conditions for the EC treatment method have been identified as follows: an inter electrode distance of 1 cm, a reaction time of 45.6061 min, a CD of 12.4173 mA/cm^2, and a maximum of 6 electrodes. Under these parameters, the calculated *ENC* is 9.855 kWh/m^3, $ELC_{\text{theoretical}}$ is 772.2 g/m^3, and ELC_{actual} is 1594.35 g/m^3, with percentage removal of 80.7% for turbidity, 57.44% for TPh, 72.32% for TKN, 56.9% for COD_{soluble}, and 56.62% for COD_{total}.

Figure 12 illustrates the relationships between the percentage removal of TKN, turbidity, TPh, COD_{soluble}, and COD_{total}, alongside the *EN*, ELC_{actual}, and $ELC_{\text{theoretical}}$ values utilizing Al electrodes. It is important to note that relatively long time will result in more *ENC* due to more ion mass loss and the consequent changes in the wastewater composition [60].

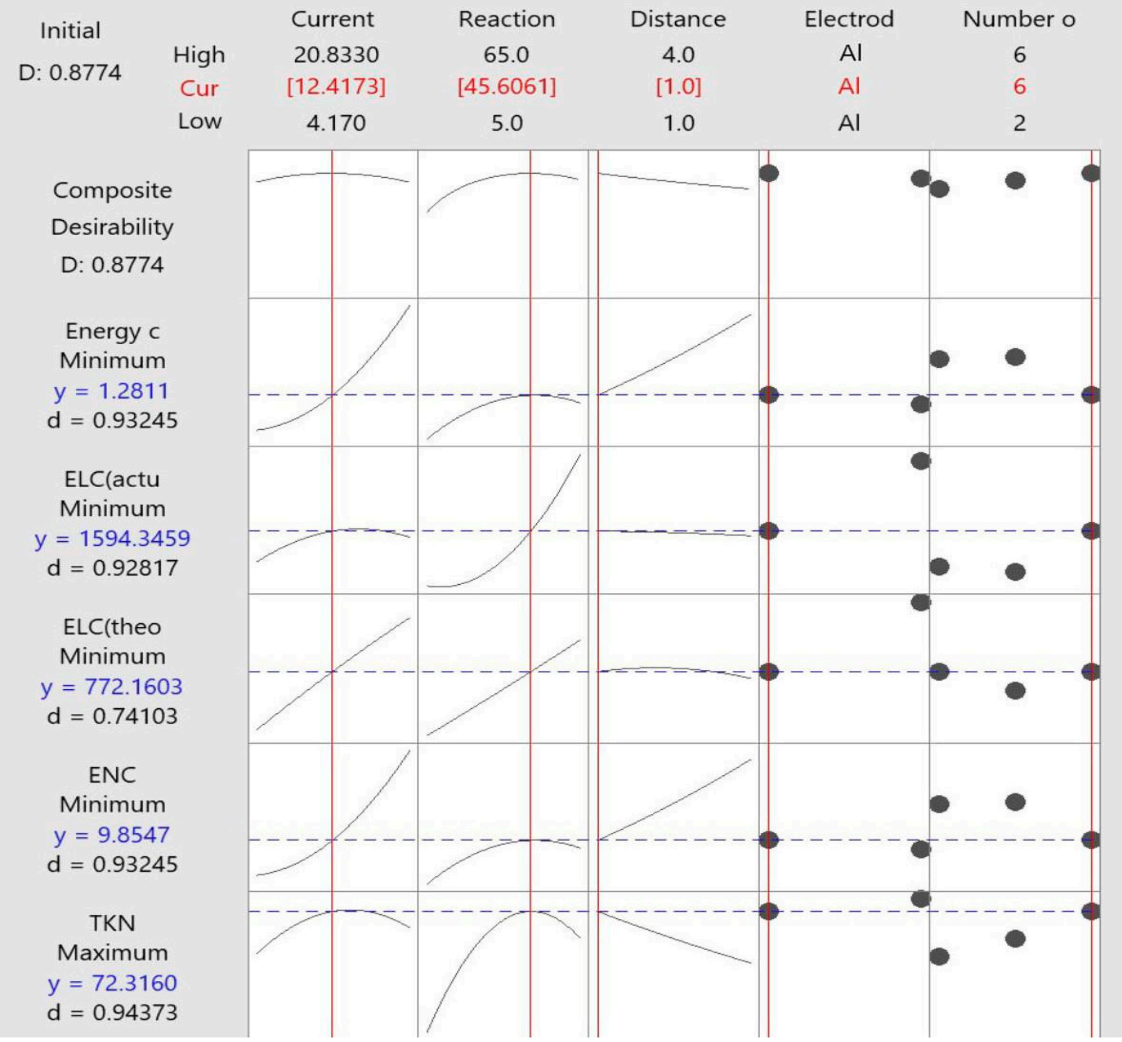

Figure 12. Optimization plot of turbidity, ENC, TKN, TPh, $COD_{soluble}$, and COD_{total} for the demonstrating the maximum removal efficiencies alongside the minimum *ENC* using Al electrode material.

In Figure 12, the optimization plot illustrates the relationships between various performance metrics such as turbidity, *ENC*, TKN, TPh, $COD_{soluble}$, and COD_{total}. Desirability is used to evaluate how well these metrics align with the desired treatment outcomes. The variable (y) indicates the performance measure related to the treatment efficiency, while (d) quantifies how desirable each outcome is, with higher values representing more favorable results.

Upon treating OMW, the estimated *OPC* for through EC under optimum conditions is approximately \$0.13/kWh, with Al priced at \$2/kg. The $ELC_{theoretical}$, in the EC cell is recorded at 0.77216 kg/m^3. The cost of adsorbent is approximately \$0.00467/m^3, sludge management is around \$0.05/m^3. Therefore, the overall *OPC* for treating OMW is about \$2.88/m^3.

3.5. Effectiveness of the Adsorption

This adsorption process results from the establishment of a low-energy zone near the surface, which increases the concentration of molecules at the surface [8,85]. In this study, the clear effluent from the EC step was used as influent to the adsorption step.

3.5.1. Adsorption Kinetics

The findings from the kinetic experiments demonstrated that the adsorption process reached equilibrium after approximately three hours. As illustrated in Figure 13, which shows the effect of contact time on TPh removal efficiency by biochar for an initial concentration of 1449.38 mg/L, the removal efficiency was measured at 23% after 180 min. This indicates that the duration of contact time was sufficient for the biochar to effectively adsorb TPh from the OMW.

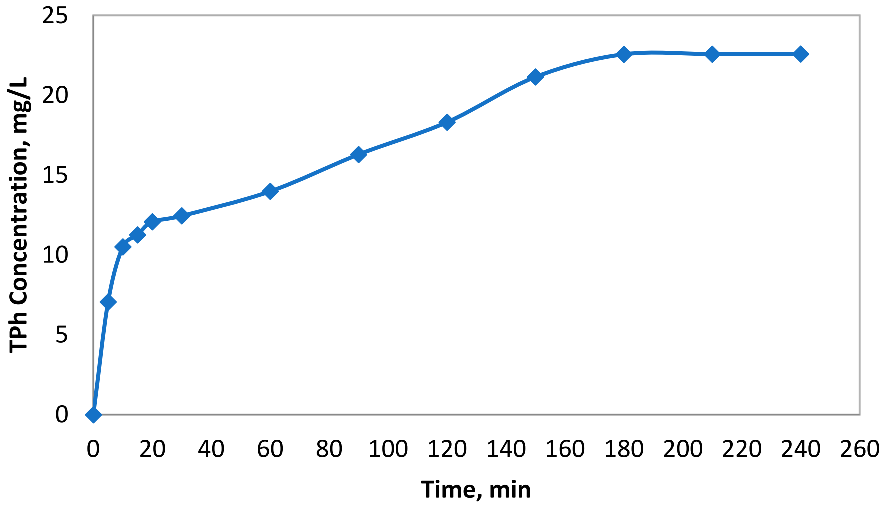

Figure 13. Effect of contact time on TPh removal efficiency by biochar for an initial concentration of 1449.38 mg/L.

The kinetic data were modeled using both pseudo-first-order and pseudo-second-order equations to understand the controlling mechanisms of the adsorption process. Figure 14a presents the results of the pseudo-first-order kinetic model, while Figure 14b illustrates the pseudo-second-order adsorption kinetics of TPh.

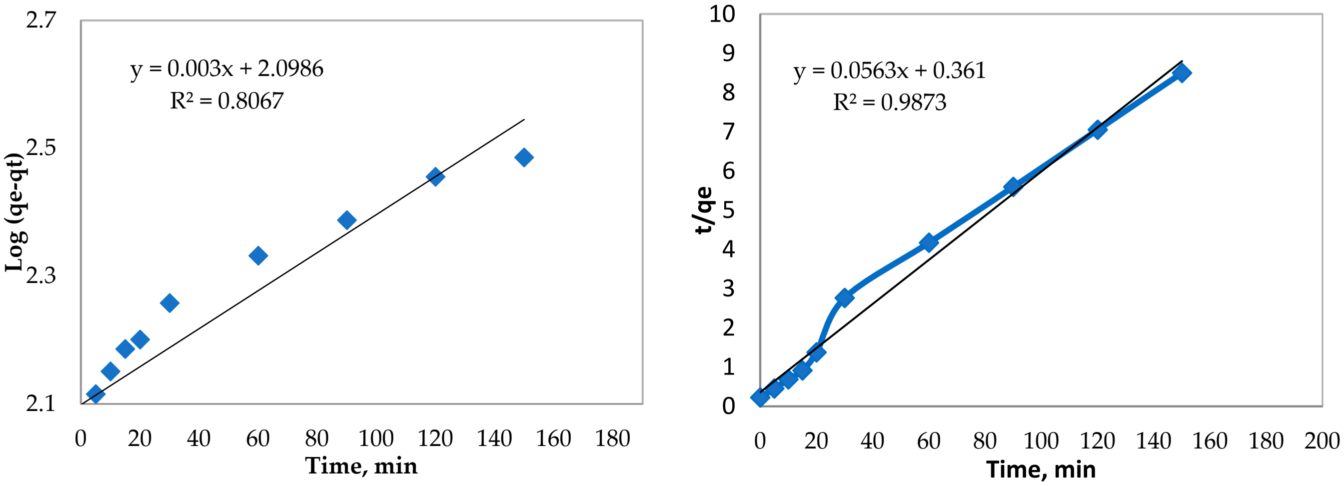

(**a**) (**b**)

Figure 14. Kinetic Adsorption of TPh: (**a**) Pseudo-first-order kinetic model, (**b**) Pseudo-second-order kinetic model.

The results showed that the adsorption of TPh onto biochar was best described by the pseudo-second-order kinetic model, which suggests that chemical sorption is a significant factor in the adsorption process. This is likely due to hydrogen bonding occurring between the active functional groups in the biochar and the hydroxyl groups of the phenolic compounds.

3.5.2. Influence of Olive Stone Particle Size

The adsorption process is strongly impacted by the adsorbent surface area available for adsorption. In this section, three particle sizes were employed: 0.075, 0.15, and 0.3 mm. These sizes were also used during the EC method under optimal conditions. Figure 15 shows the effect of OS particle size on adsorbate percentage removal.

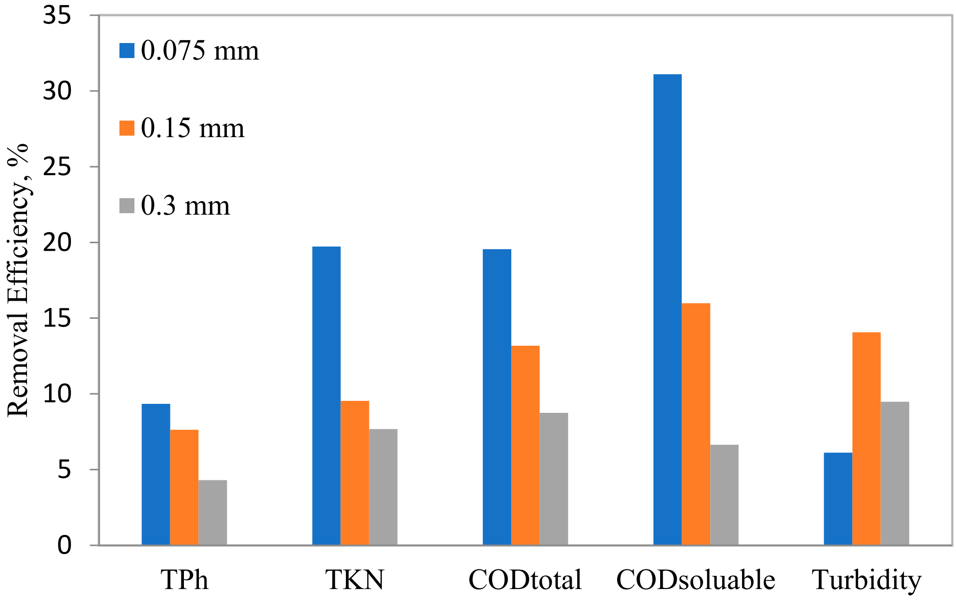

Figure 15. The percentage removal of (TPh, TKN, COD_{total}, $COD_{soluble}$, and turbidity) via adsorption process.

The findings illustrated in Figure 15 highlight the considerable effect of particle size on the percentage removal of various pollutants during the adsorption process. It is evident that for a particle size of 0.075 mm, the percentage removals are particularly high, with turbidity at 6.12%, $COD_{soluble}$ at 31.1%, COD_{total} at 19.55%, TPh at 9.33%, and TKN at 19.73%. These results suggest that the smaller particle size is most effective for pollutant removal, especially for TPh and $COD_{soluble}$, indicating that the increased surface area and reactivity of smaller particles enhance their sorption capabilities [37]. In contrast, for particles of 0.15 mm diameter, the percentage removal decreases significantly, with COD_{total} at 13.18%, $COD_{soluble}$ at 16%, TPh at 7.63%, TKN at 9.54%, and turbidity at 14.1%. On the other hand, for particles of 0.3 mm, the percentage removal further decreases, with TPh at 4.3%, TKN at 7.68%, COD_{total} at 8.75%, $COD_{soluble}$ at 6.64%, and turbidity at 9.48%. This decrease is referred to the fact that larger particles have smaller surface area compared to small ones. The marked reduction in TPh and COD removal highlights the necessity of optimizing particle size for effective treatment of OMW. In addition, this emphasizes the importance of particle size in the dynamics of sorption, as smaller particles enhance interactions and adsorption of pollutants, ultimately leading to improved treatment outcomes.

4. Hybrid Treatment System

The effectiveness of EC, adsorption, and the ECA in minimizing TPh, TKN, COD_{total}, $COD_{soluble}$, and turbidity in OMW was assessed under optimal parameters. These parameters involved a CD of 12.4 mA/cm^2, a time of 45.6 min, a 1 cm electrode spacing, 6 Al electrodes, and OS of 0.075 mm diameter. Figure 16 shows the percentage removal achieved via EC, adsorption and ECA.

Figure 16 demonstrates that the ECA combined process has the highest percentage removal of the various parameters such as TPh, TKN, COD_{total}, $COD_{soluble}$, and turbidity. The specific removal values were TPh at 61.41%, TKN at 77.8%, COD_{total} at 65.1%, $COD_{soluble}$ at 70.31%, and turbidity reduction at 81.92%. These outcomes highlight the superior effectiveness of ECA. In contrast, the percentage removal of the EC standalone process was, TPh at 57.4%, TKN at 72.3%, COD_{total} at 56.6%, $COD_{soluble}$ at 56.9%, and turbidity at 80.7%. Although these findings are significant, they do not reach the levels achieved by ECA process. Finally, the adsorption process, with an OS of 0.075 mm diameter, showed percentage removal of TPh at 9.3%, TKN at 19.7%, COD_{total} at 19.5%, $COD_{soluble}$ at 31.1%, and turbidity at 6.1%. This stark difference illustrates the limitations of using adsorption as a standalone process to treat OMW. These results are in agreement with prior study [50] that showed the advantages of ECA for enhanced removal of TPh, TKN, COD_{total}, $COD_{soluble}$, and turbidity. The high percentage removal of ECA combined system underscore its high potential for large scale applications in wastewater treatment.

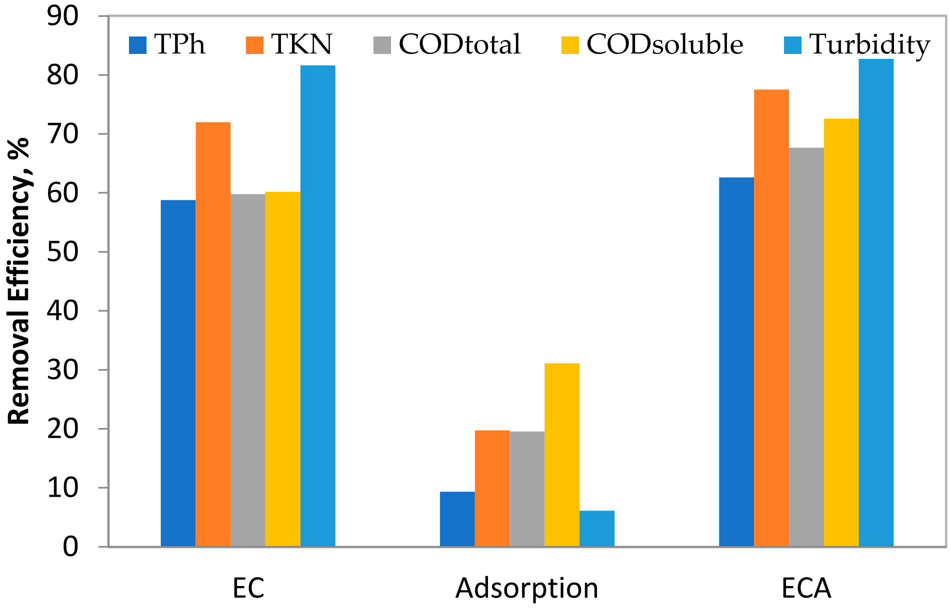

Figure 16. The percentage removal of TPh, TKN, COD_{total}, $COD_{soluble}$, and turbidity using EC, adsorption and ECA.

5. Comparison with Previous Studies

Numerous studies have investigated the combined use of EC and adsorption to treat different types of wastewaters, highlighting the effectiveness of this integrated approach in enhancing pollutant removal. Table 7 summarizes processes combining ECA to treat different wastewaters. For example, Cherifi et al. [38] focused on simulated dairy wastewater, employing Al electrodes for EC. They achieved a COD reduction of up to 78.09%. When this process was coupled with granular activated carbon (GAC), the removal rates improved significantly, with turbidity reduction reaching 99.39% and COD reduction at 87.12%. The study underscored the cost benefits associated with utilizing both techniques.

Table 7. Combined ECA processes employed in treating various types of wastewaters.

Wastewater	**Adsorbent**	**Parameters**	**Electrodes**	***ENC*, kWh/m^3**	**Cost**	**Removal Efficiency, %**	**Ref.**
Dairy wastewater	GAC	pH = 4, CD = 13.38 mA/cm^2, and GAC = 0.5 to 1.5 g	Al	—	0.360 €/m^3 and 0.746 €/m^3	92.3% of color, 99.39% of turbidity, 87.12% of COD	[38]
Dairy wastewater	GAC	GAC = 2 g/L	—	—	3 $/m^3	98 % of reduction for the COD, the BOD_5, turbidity and the greases.	[86]
Industrial Wastewater	GAC	pH = 5.0, CD = 1.388 mA cm^2, time = 30 min, and stirring speed = 300 rpm	Al	0.065 KWh/m^3	—	97% of copper.	[87]
Textile Effluent	GAC	GAC = 0.75 g/L, and time = 120 min	Al	—	—	COD, turbidity and color were, respectively, 98.33%, 100% and 98.37%.	[88]
Industrial Wastewater	Ectodermis of Opuntia	pH = 8 and CD = 45.45 A/m^2	Al	8.181 kWh	—	COD, BOD_5, color, turbidity and fecal coliforms were, respectively, 84%, 78%, 97%, 98%, and 99%.	[89]
Paper Industry Wastewater	GAC	pH of 4, CD of 1.388 Ma/cm^2, and time of 10 min	Al	0.033 KWh/m^3	—	Humic acid removal up to 93%.	[90]
Anaerobic Wastewater	GAC	pH of 6 and CD of 29.44 A/m^2	Carbon Steel/Al	1.3 kWh/m^3	—	Complete removal of COD and BOD, and turbidity (96.5%), phosphorus (97.5%) and total and thermotolerant coliforms.	[37]
Tanning wastewater	Eggshell	CD of 200 A/m^2, time of 110 min and eggshell dose of 12 g/L.	Al	1.67 kWh/kg	—	chromium of 99%	[91]
Textile Effluent	crude Tunisian clay	pH of 8.24, voltage of 70 V, and clay flow rate of 100 mL/min	Fe	—	0.75$/m^3	Color, COD and TSS removal were, respectively, 96.87%, 89.77% and 84.46%.	[92]
Beverage Industry Wastewater	Activated Carbon (AC)	2 cm electrode spacing,12 voltage, and10 g/L dose of AC.	Al	—	—	Color, COD, and TSS removal were, respectively, 98.665, 92.155, and 90.12%.	[93]
OMW	OS	CD of 15.1104 mA/cm^2, 1 cm electrode spacing, time of 53.49 min, and 6 Fe.	Fe	14.3146 kWh/m^3	3.92$/m^3	TPh, TKN, turbidity, COD_{total}, and $COD_{soluble}$ removal were, respectively, 62.63%, 77.52%, 83.73%, 72.88%, and 70.04%.	Our Previous Study [48]
OMW	OS	CD of 12.4173 mA/cm^2, 1 cm electrode spacing, time of 45.6061 min, and 6 Al.	Al	9.85466 kWh/m^3	2.88$/m^3	TPh, TKN, turbidity, COD_{total}, and $COD_{soluble}$ removal were, respectively, 61.41%, 77.78%, 81.92%, 65.1%, and 70.31%.	Current Study

In a similar vein, Eulmi et al. [86] examined dairy wastewater and optimized both EC and adsorption processes. By using a GAC dosage of 2 g/L, they reported reductions exceeding 98% in COD, BOD_5, turbidity, and grease. This highlighted the rapid effectiveness and cost-efficiency of the combined process. Barhoumi et al. [87] explored copper Fe removal and found that optimal performance was achieved at a CD of 1.388 Ma/cm^2. The addition of GAC notably decreased *ENC* and processing time, resulting in a 97% removal of copper. Aouni et al. [88] targeted textile wastewater, achieving remarkable reductions in COD (98.33%) and turbidity (100%) through the EC and GAC combination. However, they noted limitations in conductivity and total dissolved solids (TDS) removals.

Linares-Hernánde et al. [89] demonstrated the effectiveness of combining EC with biosorption for organic pollutants, achieving significant reductions and enhancing removal rates compared to standalone treatments. Barhoumi et al. [90] focused on removing humic acid, achieving up to 93% reduction through optimized EC, followed by rapid adsorption using GAC. This study highlighted the economic advantages of decreased *ENC* when combining both methods. Pizutti et al. [37] reported a conjugated system for the post-treatment of UASB effluent, where complete removal of COD and BOD was attained through optimized EC followed by adsorption, demonstrating the method's efficiency.

Both of our studies employed an integrated treatment approach that combines ECA for the treatment of OMW. Despite the consistency in methodology, significant differences emerged in electrode materials and optimization parameters, which greatly impacted overall treatment efficiency. In our previous study [48], we utilized Fe electrodes and focused primarily on the impact of temperature on the preparation of the adsorbent. The findings revealed that at an optimal temperature of 500 °C, the process yielded removal efficiencies of 54.46% for TPh and 73.25% for TKN. However, we did not incorporate a detailed analysis of *ELC* in the optimization process, which limited our ability to enhance energy efficiency and pollutant removal. Additionally, we utilized the optimal temperature identified in the previous study for preparing the adsorbent and expanded our investigation to include the effects of varying preparation times on this optimal temperature. This allowed us to explore how different preparation durations influence the physicochemical properties of the adsorbent, further enhancing its effectiveness in removing contaminants.

In our current study, we maintained the same adsorbent derived from olive seeds but switched to Al electrodes in EC process. This change in electrode material is significant because Al enhances the coagulation process due to its superior coagulant properties. By optimizing various parameters, including reaction time and CD, we achieved a reaction time of 45.6 min and a CD of 12.4 mA/cm^2. Under these optimized conditions, pollutant removal efficiencies improved markedly, achieving 80.73% for turbidity, 57.43% for TPh, and 72.32% for TKN. These enhancements reflect not only the effectiveness of the integrated approach but also the importance of electrode material in maximizing contaminant removal.

Additionally, our current research included a detailed analysis of *ENC*, calculating the *ENC* at 9.85 kWh/m^3. This represents a significant reduction from the 14.31 kWh/m^3 recorded in our previous study. The decrease in *ENC* is crucial for the economic viability of the treatment process, particularly in industrial applications where operational costs are a significant consideration. Moreover, we conducted a comprehensive evaluation of both ELC_{actual} and $ELC_{\text{theoretical}}$ in the current study. The $ELC_{\text{theoretical}}$ was determined to be 772.16 g/m^3, while the ELC_{actual} was calculated at 1594.35 g/m^3. This analysis allowed us to optimize electrode performance and enhance overall system efficiency—an aspect not fully addressed in our previous research.

6. Limitations and Future Work

6.1. Limitation

Despite the promising results of the current study, there are several limitations that need to be acknowledged:

- The wastewater used in this study contains a very high concentration of pollutants, which may lead to electrode passivation during the electrocoagulation (EC) process. This reduces the overall efficiency of the process over time and necessitates frequent maintenance or replacement of electrodes, which can hinder long-term operation.
- The EC process inherently requires significant electrical energy, particularly when treating wastewater with high pollutant loads. This increases the operational cost of the process, making it less economically feasible for large-scale applications without optimization or integration with renewable energy sources.
- The experiments in this study were performed in batch mode under controlled laboratory conditions. The results may vary under continuous or industrial-scale conditions, as operational challenges such as flow dynamics, electrode fouling, and system design could affect efficiency.

6.2. Future Prospects

Several strategies can be considered to enhance the feasibility, efficiency, and sustainability of the EC process in future work:

- Utilizing solar energy to power the EC process can significantly reduce operational costs and minimize the environmental footprint, making the process more sustainable for long-term applications.
- Transitioning from a batch to a continuous process would facilitate scale-up and improve the process efficiency by maintaining a stable treatment flow, reducing downtime, and allowing for more consistent water quality.
- Introducing a pre-treatment step, such as chemical coagulation or sedimentation, can help reduce the initial pollutant load. This would mitigate electrode passivation, improve the overall removal efficiency, and prolong electrode lifespan.
- Further studies can focus on optimizing electrode materials, current density, and reaction time to balance energy consumption and treatment efficiency, which is crucial for industrial application.
- Combining EC with other treatment technologies, such as advanced oxidation processes or membrane filtration, could improve removal efficiency for particularly challenging wastewater streams.

7. Conclusions

This research effectively employed RSM to assess the performance of EC-Adsorption as a treatment system for OMW. The adsorption step utilized OS as a sustainable adsorbent under optimized parameters. About 60 runs were conducted based on a CCD matrix, exploring various operational parameters, including number of electrodes, electrode spacing, time, and CD. The analysis revealed strong regression models with high R^2, demonstrating a reliable correlation between the predicted and experimental outcomes. At optimal conditions of 45.6 min and a CD of 12.42 mA/cm^2, and using Al electrodes, the system achieved notable percentage removal of 57.44% for TPh and 80.74% for turbidity, all while maintaining a low *ENC* at 9.85 kWh/m^3. The ECA resulted in the highest pollutant reduction efficiencies, with turbidity reduction at 81.92%, TKN removal at 77.78%, and TPh removal reaching 61.41%. This underscores the improved effectiveness of the EC-adsorption combined system. The standalone adsorption process using OS with a particle size of 0.075 mm exhibited lower percentage removal, highlighting its limitations as a treatment process for OMW. Overall, the outcomes of this study confirm that the combined ECA system enhances contaminant percentage removal and presents a promising strategy for the effective treatment of OMW.

Supplementary Materials: The following supporting information can be downloaded at: https://www.mdpi.com/article/10.3390/w18020212/s1, Figures S1–S2, Equations S1–S8.

Author Contributions: Conceptualization, A.J., T.M.A.-Z., Z.A.-Q. and E.A.; methodology, A.J., T.M.A.-Z. and Z.A.-Q.; formal analysis, A.J., T.M.A.-Z., Z.A.-Q. and E.A.-K.; investigation, T.M.A.-Z. and Z.A.-Q.; resources, A.J., T.M.A.-Z., Z.A.-Q., E.A.-K. and E.A.; data curation, A.J., T.M.A.-Z., Z.A.-Q., E.A.-K., M.M. and E.A.; writing—original draft preparation, T.M.A.-Z.; writing—review and editing, T.M.A.-Z. and Z.A.-Q. All authors have read and agreed to the published version of the manuscript.

Funding: This study was financially supported by "ABDUL HAMEED SHOMAN FOUNDATION," "the Jordanian Higher Council for Science and Technology (HCST) under CYCLOLIVE Project ID 1977 one of PRIMA II projects," and "Deanship of Scientific Research at The University of Jordan.".

Data Availability Statement: The original contributions presented in this study are included in the article. Further inquiries can be directed to the corresponding authors.

Conflicts of Interest: The authors declare no conflicts of interest.

References

1. Christian, D.; Gaekwad, A.; Dani, H.; Shabiimam, M.A.; Kandya, A. Recent Techniques of Textile Industrial Wastewater Treatment: A Review. *Mater. Today Proc.* **2023**, *77*, 277–285. [CrossRef]
2. Jamrah, A.; Al-Zghoul, T.M.; Darwish, M.M. A Comprehensive Review of Combined Processes for Olive Mill Wastewater Treatments. *Case Stud. Chem. Environ. Eng.* **2023**, *8*, 100493. [CrossRef]
3. Baarimah, A.O.; Bazel, M.A.; Alaloul, W.S.; Alazaiza, M.Y.D.; Al-Zghoul, T.M.; Almuhaya, B.; Khan, A.; Mushtaha, A.W. Artificial Intelligence in Wastewater Treatment: Research Trends and Future Perspectives through Bibliometric Analysis. *Case Stud. Chem. Environ. Eng.* **2024**, *10*, 100926. [CrossRef]
4. UNESCO. *The United Nations World Water Development Report 2025*; UNESCO: Paris, France, 2025.
5. Amdeha, E. Biochar-Based Nanocomposites for Industrial Wastewater Treatment via Adsorption and Photocatalytic Degradation and the Parameters Affecting These Processes. *Biomass Convers. Biorefinery* **2024**, *14*, 23293–23318. [CrossRef]
6. Naidu, R.; Biswas, B.; Willett, I.R.; Cribb, J.; Kumar Singh, B.; Paul Nathanail, C.; Coulon, F.; Semple, K.T.; Jones, K.C.; Barclay, A.; et al. Chemical Pollution: A Growing Peril and Potential Catastrophic Risk to Humanity. *Environ. Int.* **2021**, *156*, 106616. [CrossRef] [PubMed]
7. Alazaiza, M.Y.D.; Alzghoul, T.M.; Amr, S.A.; Bangalore Ramu, M.; Nassani, D.E. Bibliometric Insights into Car Wash Wastewater Treatment Research: Trends and Perspectives. *Water* **2024**, *16*, 2034. [CrossRef]
8. Al-Qodah, Z.; Al-Zghoul, T.M.; Jamrah, A. The Performance of Pharmaceutical Wastewater Treatment System of Electrocoagulation Assisted Adsorption Using Perforated Electrodes to Reduce Passivation. *Environ. Sci. Pollut. Res.* **2024**, *31*, 20434–20448. [CrossRef]
9. Faraj, H.; Jamrah, A.; Al-Omari, S.; Al-Zghoul, T.M. Optimization of an Electrocoagulation-Assisted Adsorption Treatment System for Dairy Wastewater. *Case Stud. Chem. Environ. Eng.* **2024**, *9*, 100574. [CrossRef]
10. Buthiyappan, A.; Abdul Raman, A.A. Energy Intensified Integrated Advanced Oxidation Technology for the Treatment of Recalcitrant Industrial Wastewater. *J. Clean. Prod.* **2019**, *206*, 1025–1040. [CrossRef]
11. Lin, S.; Mackey, H.R.; Hao, T.; Guo, G.; van Loosdrecht, M.C.M.; Chen, G. Biological Sulfur Oxidation in Wastewater Treatment: A Review of Emerging Opportunities. *Water Res.* **2018**, *143*, 399–415. [CrossRef]
12. Karthikeyan, K.T.; Nithya, A.; Jothivenkatachalam, K. Photocatalytic and Antimicrobial Activities of Chitosan-TiO2 Nanocomposite. *Int. J. Biol. Macromol.* **2017**, *104*, 1762–1773. [CrossRef]
13. Jamrah, A.; Al-Zghoul, T.; Baarimah, A.O.; Al-Karablieh, E. A Bibliometric Analysis of Olive Mill Wastewater Treatment Methods from 1988 to 2023. *Case Stud. Chem. Environ. Eng.* **2024**, *9*, 100736. [CrossRef]
14. Haddad, K.; Jeguirim, M.; Jellali, S.; Thevenin, N.; Ruidavets, L.; Limousy, L. Biochar Production from Cypress Sawdust and Olive Mill Wastewater: Agronomic Approach. *Sci. Total Environ.* **2021**, *752*, 141713. [CrossRef]

15. Jyia, H.; Mohssine, A.; Belouafa, S.; EL Harfaoui, S.; Zmirli, Z.; Sallek, B.; Khalid, D.; Chaair, H. Modeling and Optimization of Olive Mill Wastewater Dephenolization by a Process Combining Coagulation and Advanced Oxidation Using an Activated Lime Coagulant and Hydrogen Peroxide. *Environ. Nanotechnology, Monit. Manag.* **2024**, *21*, 100929. [CrossRef]
16. Gebreyohannes, A.Y.; Mazzei, R.; Giorno, L. Trends and Current Practices of Olive Mill Wastewater Treatment: Application of Integrated Membrane Process and Its Future Perspective. *Sep. Purif. Technol.* **2016**, *162*, 45–60. [CrossRef]
17. Alkhalidi, A.; Halaweh, G.; Khawaja, M.K. Recommendations for Olive Mills Waste Treatment in Hot and Dry Climate. *J. Saudi Soc. Agric. Sci.* **2023**, *22*, 361–373. [CrossRef]
18. Barbera, A.C.; Maucieri, C.; Cavallaro, V.; Ioppolo, A.; Spagna, G. Effects of Spreading Olive Mill Wastewater on Soil Properties and Crops, a Review. *Agric. Water Manag.* **2013**, *119*, 43–53. [CrossRef]
19. Domingues, E.; Lincho, J.; Fernandes, M.J.; Gomes, J.; Martins, R.C. Low-Cost Materials for Swine Wastewater Treatment Using Adsorption and Fenton's Process. *Environ. Sci. Pollut. Res.* **2023**, *32*, 10519–10529. [CrossRef] [PubMed]
20. Ochando-Pulido, J.M.; Pimentel-Moral, S.; Verardo, V.; Martinez-Ferez, A. A Focus on Advanced Physico-Chemical Processes for Olive Mill Wastewater Treatment. *Sep. Purif. Technol.* **2017**, *179*, 161–174. [CrossRef]
21. Bombino, G.; Andiloro, S.; Folino, A.; Lucas-Borja, M.E.; Zema, D.A. Short-Term Effects of Olive Oil Mill Wastewater Application on Soil Water Repellency. *Agric. Water Manag.* **2021**, *244*, 106563. [CrossRef]
22. Vaz, T.; Quina, M.M.J.; Martins, R.C.; Gomes, J. Olive Mill Wastewater Treatment Strategies to Obtain Quality Water for Irrigation: A Review. *Sci. Total Environ.* **2024**, *931*, 172676. [CrossRef] [PubMed]
23. El Moussaoui, T. Studies on the Activated Sludge Process Crucial Parameters Controlling Olive Mill Wastewater Treatment. *Sci. Total Environ.* **2022**, *838*, 156455. [CrossRef]
24. Adhoum, N.; Monser, L. Decolourization and Removal of Phenolic Compounds from Olive Mill Wastewater by Electrocoagulation. *Chem. Eng. Process. Process Intensif.* **2004**, *43*, 1281–1287. [CrossRef]
25. Manthos, G.; Zagklis, D.; Papavasileiou, V.; Gkountou, N.A.; Saita, Z.; Zafiri, C.; Kornaros, M. High-Rate Upflow Anaerobic Sludge Blanket Bioreactor for the Treatment of Olive Mill Effluents: Laboratory and Pilot Scale Systems Investigation. *Renew. Energy* **2023**, *217*, 119215. [CrossRef]
26. Bouigua, H.; Bakali, R.; Jaber, H.; El Kabous, K.; Choukri, S.; Elyachioui, M.; Ouhssine, M. A Remarkable Step in the Aerobic Biological Treatment of Olive Mill Wastewater (OMW): A Combination of Selected Microbial Strains That Enhance Their Decolorization and Depollution. *E3S Web Conf.* **2024**, *527*, 02007. [CrossRef]
27. Rocha, K.O.; Brandão, F.; átia Mendes, C.; Carvalho, M.G.V.S.; Mazierski, P.; Zaleska-Medynska, A.; Gomes, J.; Martins, R.C.; Domingues, E. Olive Mill Waste Bio-Based Catalyst Application in Advanced Oxidation Processes for Wastewater Treatment. *Catal. Today* **2024**, *432*, 114618. [CrossRef]
28. Agabo-García, C.; Repetto, G.; Albqmi, M.; Hodaifa, G. Evaluation of the Olive Mill Wastewater Treatment Based on Advanced Oxidation Processes (AOPs), Flocculation, and Filtration. *J. Environ. Chem. Eng.* **2023**, *11*, 109789. [CrossRef]
29. Tayeh, Y.A. A Comprehensive Review of Reverse Osmosis Desalination: Technology, Water Sources, Membrane Processes, Fouling, and Cleaning. *Desalin. Water Treat.* **2024**, *320*, 100882. [CrossRef]
30. Ait-Hmane, A.; Mandi, L.; Ouazzani, N.; Ouhammou, M.; El Moussaoui, T.; Ait hammou, H.; Assabbane, A. Treatment of Olive Mill Wastewater by Coagulation–Flocculation with Aluminum Sulphate/Aluminum Polyhydroxichlorosulfate and Effect on Phytotoxicity. *Desalin. Water Treat.* **2024**, *318*, 100340. [CrossRef]
31. Al-Zghoul, T.M.; Al-Qodah, Z.; Al-Jamrah, A. Performance, Modeling, and Cost Analysis of Chemical Coagulation-Assisted Solar Powered Electrocoagulation Treatment System for Pharmaceutical Wastewater. *Water* **2023**, *15*, 980. [CrossRef]
32. Alazaiza, M.Y.D.; Alzghoul, T.M.; Nassani, D.E.; Bashir, M.J.K. Natural Coagulants for Sustainable Wastewater Treatment: Current Global Research Trends. *Processes* **2025**, *13*, 1754. [CrossRef]
33. Yazici Guvenc, S.; Tunc, S. Alternative Treatment of Olive Mill Wastewater by Combined Sulfate Radical-based Advanced Electrocoagulation Processes. *Water Environ. Res.* **2023**, *95*, e10951. [CrossRef]
34. Khandegar, V.; Acharya, S.; Jain, A.K. Data on Treatment of Sewage Wastewater by Electrocoagulation Using Punched Aluminum Electrode and Characterization of Generated Sludge. *Data Br.* **2018**, *18*, 1229–1238. [CrossRef]
35. Tahreen, A.; Jami, M.S.; Ali, F. Role of Electrocoagulation in Wastewater Treatment: A Developmental Review. *J. Water Process Eng.* **2020**, *37*, 101440. [CrossRef]
36. Hamimed, S.; Bousdira, F.; Harkas, M. Novel Development of Sustainable Nanofertilizers from Olive Pomace Waste. *Biocatal. Agric. Biotechnol.* **2025**, *66*, 103616. [CrossRef]
37. Pizutti, J.T.; de Cassia dos Santos, R.; Hemkemeier, M.; Piccin, J.S. Electrocoagulation Coupled Adsorption for Anaerobic Wastewater Post-Treatment and Reuse Purposes. *Desalin. Water Treat.* **2019**, *160*, 144–152. [CrossRef]
38. Cherifi, M.; Guenfoud, S.; Bendaia, M.; Hazourli, S.; Laefer, D.F.; Leclerc, J.P.; Mecibah, W. Comparative Study between Electrocoagulation Used Separately and Coupled with Adsorption for Dairy Wastewater Treatment Using Response Surface Methodology Design. *Desalin. Water Treat.* **2021**, *223*, 235–245. [CrossRef]

39. Zhou, H.; Wei, C.; Zhang, F.; Liao, J.; Hu, Y.; Wu, H. Energy-Saving Optimization of Coking Wastewater Treated by Aerobic Bio-Treatment Integrating Two-Stage Activated Carbon Adsorption. *J. Clean. Prod.* **2018**, *175*, 467–476. [CrossRef]
40. Jamrah, A.; Al-Jawaldeh, H.; Al-Zghoul, T.M.; Hamaideh, A.; Darwish, M.M.; Al-Karablieh, E. Olive Pits Activated Carbon as an Effective Adsorbent for Water Treatment Using H_3PO_4 and H_2SO_4 Activating Agents. *Water Conserv. Manag.* **2024**, *8*, 415–419. [CrossRef]
41. El-Sheikh, A.H.; Newman, A.P.; Al-Daffaee, H.K.; Phull, S.; Cresswell, N. Characterization of Activated Carbon Prepared from a Single Cultivar of Jordanian Olive Stones by Chemical and Physicochemical Techniques. *J. Anal. Appl. Pyrolysis* **2004**, *71*, 151–164. [CrossRef]
42. Akl, M.A.; AbdElFatah, M.; AbdElnasser, Y.; AbdElnasser, S. Removal of Iron and Manganese in Water Samples Using Activated Carbon Derived from Local Agro-Residues. *J. Chem. Eng. Process Technol.* **2013**, *4*, 154. [CrossRef]
43. Al-Balushi, K.; Revanuru, S.; Sajjala, S.R. Preparation of Activated Carbon from Date Seeds and Evaluation of Its Applications. In Proceedings of the International Conference on Civil, Disaster Management and Environmental Sciences (CDMES-17), Bali, Indonesia, 8–9 February 2017; pp. 2–3.
44. Görmez, F.; Görmez, Ö.; Yabalak, E.; Gözmen, B. Application of the Central Composite Design to Mineralization of Olive Mill Wastewater by the Electro/FeII/Persulfate Oxidation Method. *SN Appl. Sci.* **2020**, *2*, 178. [CrossRef]
45. Patel, S.R.; Pathan, M.; Nayak, M.G.; Parikh, S.P.; Rajaraman, T.S.; Ambegaonkar, N.J.; Trivedi, J.B. Energy Efficient Electrocoagulation Using Brass Electrode for Simultaneous Nickel and Chromium Removal from Synthetic Wastewater: Cost and Parametric Evaluation. *Results Eng.* **2024**, *22*, 102361. [CrossRef]
46. Kalderis, D.; Kayan, B.; Akay, S.; Kulaksız, E.; Gözmen, B. Adsorption of 2,4-Dichlorophenol on Paper Sludge/Wheat Husk Biochar: Process Optimization and Comparison with Biochars Prepared from Wood Chips, Sewage Sludge and Hog Fuel/Demolition Waste. *J. Environ. Chem. Eng.* **2017**, *5*, 2222–2231. [CrossRef]
47. Yabalak, E.; Görmez, Ö.; Gizir, A.M. Subcritical Water Oxidation of Propham by H 2 O 2 Using Response Surface Methodology (RSM). *J. Environ. Sci. Health Part B* **2018**, *53*, 334–339. [CrossRef] [PubMed]
48. Jamrah, A.; Al-Zghoul, T.M.; Al-Qodah, Z.; Al-Karablieh, E. Performance of Combined Olive Mills Wastewater Treatment System: Electrocoagulation-Assisted Adsorption as a Post Polishing Sustainable Process. *Water* **2025**, *17*, 1697. [CrossRef]
49. Baird, R.; Rice, E.; Eaton, A. *Standard Methods for the Examination of Water and Wastewaters*, 23rd ed.; Water Environment Federation, Chair Eugene W. Rice, American Public Health Association Andrew D. Eaton, American Water Works Association; American Water Works Association: Denver, CO, USA, 2017.
50. Castañeda-Díaz, J.; Pavón-Silva, T.; Gutiérrez-Segura, E.; Colín-Cruz, A. Electrocoagulation-Adsorption to Remove Anionic and Cationic Dyes from Aqueous Solution by PV-Energy. *J. Chem.* **2017**, *2017*, 1–14. [CrossRef]
51. Halalsheh, M.; Koppes, J.; Denelzen, J.; Zeeman, G.; Fayyad, M.; Lettinga, G. Effect of SRT and Temperature on Biological Conversions and the Related Scum-Forming Potential. *Water Res.* **2005**, *39*, 2475–2482. [CrossRef]
52. Behbahani, M.; Alavi, M.M.; Arami, M. A Comparison between Aluminum and Iron Electrodes on Removal of Phosphate from Aqueous Solutions by Electrocoagulation Process. *Int. J. Environ. Res.* **2011**, *5*, 403–412.
53. Abrane, R.; Hazourli, S.; Eulmi, A. Comparative Study between Electrocoagulation and Adsorption on the Opuntia Ficus Indica Powder for Industrial Dairy Wastewater Treatment. *Desalin. Water Treat.* **2021**, *228*, 153–164. [CrossRef]
54. Amani-Ghadim, A.R.; Aber, S.; Olad, A.; Ashassi-Sorkhabi, H. Optimization of Electrocoagulation Process for Removal of an Azo Dye Using Response Surface Methodology and Investigation on the Occurrence of Destructive Side Reactions. *Chem. Eng. Process. Process Intensif.* **2013**, *64*, 68–78. [CrossRef]
55. Hamid, M.A.A.; Aziz, H.A.; Yusoff, M.S.; Rezan, S.A. Optimization and Analysis of Zeolite Augmented Electrocoagulation Process in the Reduction of High-Strength Ammonia in Saline Landfill Leachate. *Water* **2020**, *12*, 247. [CrossRef]
56. Ankoliya, D.; Mudgal, A.; Sinha, M.K.; Patel, V.; Patel, J. Application of Electrocoagulation Process for the Treatment of Dairy Wastewater: A Mini Review. *Mater. Today Proc.* **2023**, *77*, 117–124. [CrossRef]
57. Martínez-Huitle, C.A.; Brillas, E. Decontamination of Wastewaters Containing Synthetic Organic Dyes by Electrochemical Methods: A General Review. *Appl. Catal. B Environ.* **2009**, *87*, 105–145. [CrossRef]
58. Ilhan, F.; Kurt, U.; Apaydin, O.; Gonullu, M.T. Treatment of Leachate by Electrocoagulation Using Aluminum and Iron Electrodes. *J. Hazard. Mater.* **2008**, *154*, 381–389. [CrossRef]
59. Galanakis, C.M. Olive Fruit Dietary Fiber: Components, Recovery and Applications. *Trends Food Sci. Technol.* **2011**, *22*, 175–184. [CrossRef]
60. Shahawy, A.E.; Ahmed, I.A.; Nasr, M.; Ragab, A.H.; Al-Mhyawi, S.R.; Elamin, K.M.A. Organic Pollutants Removal from Olive Mill Wastewater Using Electrocoagulation Process via Central Composite Design (CCD). *Water* **2021**, *13*, 3522. [CrossRef]
61. Elayeb, R.; Njehi, M.; Majdoub, H.; Trigui, M.; Achour, S. Optimization of the Electrocoagulation Process by Central Composite Design for Olive Mill Wastewater Decolorization and Removal of Polyphenols. *Int. Res. J. Adv. Eng. Sci.* **2021**, *6*, 182–200.
62. Fakhfakh, F.; Raissi, S.; Kriaa, K.; Maatki, C.; Kolsi, L.; Hadrich, B. Modeling and Optimization of a Green Process for Olive Mill Wastewater Treatment. *Water* **2024**, *16*, 327. [CrossRef]

63. Khani, M.R.; Mahdizadeh, H.; Kannan, K.; Kalankesh, L.R.; Kamarehei, B.; Baneshi, M.M.; Shahamat, Y.D. Olive Mill Wastewater (OMW) Treatment by Hybrid Processes of Electrocoagulation/Catalytic Ozonation and Biodegradation. *Environ. Eng. Manag. J.* **2020**, *19*, 1401–1410. [CrossRef]
64. De Carluccio, M.; Barboza, P.; Attarian, P.; Ahangarnokolaei, M.A.; Rizzo, L. Olive Mill Wastewater Co-Treatment: Effect of (Electro)Fenton Processes and Dilution Ratio on Moving Bed Biofilm Reactor Performance. *J. Clean. Prod.* **2024**, *447*, 141526. [CrossRef]
65. Ayoub, S.; Al-Absi, K.; Al-Shdiefat, S.; Al-Majali, D.; Hijazean, D. Effect of Olive Mill Wastewater Land-Spreading on Soil Properties, Olive Tree Performance and Oil Quality. *Sci. Hortic.* **2014**, *175*, 160–166. [CrossRef]
66. Al-Qodah, Z.; Al-Bsoul, A.; Assirey, E.; Al-Shannag, M. Combined Ultrasonic Irradiation and Aerobic Biodegradation Treatment for Olive Mills Wastewaters. *Environ. Eng. Manag. J.* **2014**, *8*, 2109–2118. [CrossRef]
67. Abdelhadi, S.O.; Dosoretz, C.G.; Rytwo, G.; Gerchman, Y.; Azaizeh, H. Production of Biochar from Olive Mill Solid Waste for Heavy Metal Removal. *Bioresour. Technol.* **2017**, *244*, 759–767. [CrossRef]
68. Abid, N.; Masmoudi, M.A.; Megdiche, M.; Barakat, A.; Ellouze, M.; Chamkha, M.; Ksibi, M.; Sayadi, S. Biochar from Olive Mill Solid Waste as an Eco-Friendly Adsorbent for the Removal of Polyphenols from Olive Mill Wastewater. *Chem. Eng. Res. Des.* **2022**, *181*, 384–398. [CrossRef]
69. Elhajjouji, H.; Fakharedine, N.; Aitbaddi, G.; Winterton, P.; Bailly, J.; Revel, J.; Hafidi, M. Treatment of Olive Mill Waste-Water by Aerobic Biodegradation: An Analytical Study Using Gel Permeation Chromatography, Ultraviolet–Visible and Fourier Transform Infrared Spectroscopy. *Bioresour. Technol.* **2007**, *98*, 3513–3520. [CrossRef]
70. Hafidi, M.; Amir, S.; Revel, J.-C. Structural Characterization of Olive Mill Waster-Water after Aerobic Digestion Using Elemental Analysis, FTIR and 13C NMR. *Process Biochem.* **2005**, *40*, 2615–2622. [CrossRef]
71. Varank, G.; Sabuncu, M.E. Application of Central Composite Design Approach for Dairy Wastewater Treatment by Electrocoagulation Using Iron and Aluminum Electrodes: Modeling and Optimization. *Desalin. Water Treat.* **2015**, *56*, 33–54. [CrossRef]
72. Holt, P.K.; Barton, G.W.; Wark, M.; Mitchell, C.A. A Quantitative Comparison between Chemical Dosing and Electrocoagulation. *Colloids Surfaces A Physicochem. Eng. Asp.* **2002**, *211*, 233–248. [CrossRef]
73. Duan, J.; Gregory, J. Coagulation by Hydrolysing Metal Salts. *Adv. Colloid Interface Sci.* **2003**, *100–102*, 475–502. [CrossRef]
74. Nasrullah, M.; Siddique, M.N.I.; Zularisam, A.W. Effect of High Current Density in Electrocoagulation Process for Sewage Treatment. *Asian J. Chem.* **2014**, *26*, 4281–4285. [CrossRef]
75. Behera, U.S.; Poddar, S.; Byun, H.-S. Electrocoagulation Treatment of Wastewater Collected from Haldia Industrial Region: Performance Evaluation and Comparison of Process Optimization. *Water Res.* **2025**, *268*, 122716. [CrossRef]
76. Titchou, F.E.; Zazou, H.; Afanga, H.; El Gaayda, J.; Akbour, R.A.; Hamdani, M. Removal of Persistent Organic Pollutants (POPs) from Water and Wastewater by Adsorption and Electrocoagulation Process. *Groundw. Sustain. Dev.* **2021**, *13*, 100575. [CrossRef]
77. Holt, P.K.; Barton, G.W.; Mitchell, C.A. The Future for Electrocoagulation as a Localised Water Treatment Technology. *Chemosphere* **2005**, *59*, 355–367. [CrossRef]
78. Janpoor, F.; Torabian, A.; Khatibikamal, V. Treatment of Laundry Waste-water by Electrocoagulation. *J. Chem. Technol. Biotechnol.* **2011**, *86*, 1113–1120. [CrossRef]
79. Niazmand, R.; Jahani, M.; Sabbagh, F.; Rezania, S. Optimization of Electrocoagulation Conditions for the Purification of Table Olive Debittering Wastewater Using Response Surface Methodology. *Water* **2020**, *12*, 1687. [CrossRef]
80. Assas, N.; Ayed, L.; Marouani, L.; Hamdi, M. Decolorization of Fresh and Stored-Black Olive Mill Wastewaters by Geotrichum Candidum. *Process Biochem.* **2002**, *38*, 361–365. [CrossRef]
81. Safaa, K.R.; Anouzla, A.; Abrouki, Y.; Loukili, H.; Kastali, M.; Souabi, S. Management of Olive Oil Mill Wastewater in Morocco. In *Wastewater from Olive Oil Production: Environmental Impacts, Treatment and Valorisation*; Springer International Publishing: Cham, Switzerland, 2023; pp. 183–212.
82. Tezcan Ün, Ü.; Uğur, S.; Koparal, A.S.; Bakır Öğütveren, Ü. Electrocoagulation of Olive Mill Wastewaters. *Sep. Purif. Technol.* **2006**, *52*, 136–141. [CrossRef]
83. Lemlikchi, W.; Khaldi, S.; Mecherri, M.O.; Lounici, H.; Drouiche, N. Degradation of Disperse Red 167 Azo Dye by Bipolar Electrocoagulation. *Sep. Sci. Technol.* **2012**, *47*, 1682–1688. [CrossRef]
84. Bazrafshan, E.; Alipour, M.R.; Mahvi, A.H. Textile Wastewater Treatment by Application of Combined Chemical Coagulation, Electrocoagulation, and Adsorption Processes. *Desalin. Water Treat.* **2016**, *57*, 9203–9215. [CrossRef]
85. Awad, A. Removal Efficiency, Metal Uptake, and Breakthrough Curve of Aqueous Lead Ions Removal Using Olive Stone Waste. *Results Eng.* **2024**, *22*, 102311. [CrossRef]
86. Eulmi, A.; Hazourli, S.; Abrane, R.; Bendaia, M.; Aitbara, A.; Touahria, S.; Chérifi, M. Evaluation of Electrocoagulation and Activated Carbon Adsorption Techniques Used Separately or Coupled to Treat Wastewater from Industrial Dairy. *Int. J. Chem. React. Eng.* **2019**, *17*, 20180229. [CrossRef]
87. Barhoumi, A.; Ncib, S.; Bouguerra, W.; Hamrouni, B.; Elaloui, E. Combining Adsorption on Activated Carbon with Electrocoagulation Process for Copper Removal from Used Water. *Desalin. Water Treat.* **2017**, *83*, 212–221. [CrossRef]

88. Aouni, A.; Lafi, R.; Hafiane, A. Feasibility Evaluation of Combined Electrocoagulation/Adsorption Process by Optimizing Operating Parameters Removal for Textile Wastewater Treatment. *Desalin. Water Treat.* **2017**, *60*, 78–87. [CrossRef]
89. Linares-Hernández, I.; Barrera-Díaz, C.; Roa-Morales, G.; Bilyeu, B.; Ureña-Núñez, F. A Combined Electrocoagulation–Sorption Process Applied to Mixed Industrial Wastewater. *J. Hazard. Mater.* **2007**, *144*, 240–248. [CrossRef]
90. Barhoumi, A.; Ncib, S.; Chibani, A.; Brahmi, K.; Bouguerra, W.; Elaloui, E. High-Rate Humic Acid Removal from Cellulose and Paper Industry Wastewater by Combining Electrocoagulation Process with Adsorption onto Granular Activated Carbon. *Ind. Crops Prod.* **2019**, *140*, 111715. [CrossRef]
91. Elabbas, S.; Adjeroud, N.; Mandi, L.; Berrekhis, F.; Pons, M.N.; Leclerc, J.P.; Ouazzani, N. Eggshell Adsorption Process Coupled with Electrocoagulation for Improvement of Chromium Removal from Tanning Wastewater. *Int. J. Environ. Anal. Chem.* **2022**, *102*, 2966–2978. [CrossRef]
92. Hendaoui, K.; Trabelsi-Ayadi, M.; Ayari, F. Optimization of Continuous Electrocoagulation-Adsorption Combined Process for the Treatment of a Textile Effluent. *Chinese J. Chem. Eng.* **2022**, *44*, 310–320. [CrossRef]
93. Muryanto, M.; Marlina, E.; Sari, A.A.; Harimawan, A.; Sudarno, S. Treatment of Beverage Industry Wastewater Using a Combination of Electrocoagulation and Adsorption Processes. In Proceedings of the 4th International Symposium On Applied Chemistry 2018, Banten, Indonesia, 1–2 November 2018; p. 020004. [CrossRef]

https://doi.org/10.3390/w18020212